2021-07

Wind speed and mesoscale features drive net autotrophy in the South Atlantic Ocean

Ford, D

10.1016/j.rse.2021.112435
Remote Sensing of Environment: an interdisciplinary journal
Elsevier

Remote Sensing of Environment 260 (2021) 112435

Contents lists available at ScienceDirect

Remote Sensing of Environment

journal homepage: www.elsevier.com/locate/rse

Wind speed and mesoscale features drive net autotrophy in the South Atlantic Ocean

Daniel Ford [a,b,*], Gavin H. Tilstone [a], Jamie D. Shutler [b], Vassilis Kitidis [a], Polina Lobanova [c], Jill Schwarz [d], Alex J. Poulton [e], Pablo Serret [f], Tarron Lamont [g,h,j], Mateus Chuqui [i], Ray Barlow [h,j], Jose Lozano [f], Milton Kampel [k], Frederico Brandini [i]

[a] Plymouth Marine Laboratory, Plymouth, UK
[b] College of Life and Environmental Sciences, University of Exeter, UK
[c] St. Petersburg State University, St. Petersburg, Russia
[d] School of Biological and Marine Sciences, University of Plymouth, Plymouth, UK
[e] Lyell Centre for Earth & Marine Science & Technology, Heriot-Watt University, Edinburgh, UK
[f] Centro de Investigación Mariña, RE, Universidad de Vigo, Spain
[g] Oceans & Coasts Research, Department of Environment, Forestry & Fisheries, Cape Town, South Africa
[h] Bayworld Centre for Research & Education, Cape Town, South Africa
[i] Laboratory of Marine Biogeochemistry, Department of Biological Oceanography, Oceanographic Institute, University of São Paulo, Brazil
[j] Marine Research Institute & Department of Oceanography, University of Cape Town, South Africa
[k] National Institute for Space Research, São José dos Campos, São Paulo, Brazil

ARTICLE INFO

Editor: Menghua Wang

Keywords:
MODIS-A
in situ uncertainty
Ocean colour
Environmental drivers
South Atlantic Ocean
Ocean metabolism

ABSTRACT

A comprehensive *in situ* dataset of chlorophyll *a* (Chl *a*; $N = 18{,}001$), net primary production (NPP; $N = 165$) and net community production (NCP; $N = 95$), were used to evaluate the performance of Moderate Resolution Imaging Spectroradiometer on Aqua (MODIS-A) algorithms for these parameters, in the South Atlantic Ocean, to facilitate the accurate generation of satellite NCP time series. For Chl *a*, five algorithms were tested using MODIS-A data, and OC3-CI performed best, which was subsequently used to compute NPP. Of three NPP algorithms tested, a Wavelength Resolved Model (WRM) was the most accurate, and was therefore used to estimate NCP with an empirical relationship between NCP with NPP and sea surface temperature (SST). A perturbation analysis was deployed to quantify the range of uncertainties introduced in satellite NCP from input parameters. The largest reductions in the uncertainty of satellite NCP came from MODIS-A derived NPP using the WRM (40%) and MODIS-A Chl *a* using OC3-CI (22%).

The most accurate NCP algorithm, was used to generate a 16 year time series (2002 to 2018) from MODIS-A to assess climate and environmental drivers of NCP across the South Atlantic basin. Positive correlations between wind speed anomalies and NCP anomalies were observed in the central South Atlantic Gyre (SATL), and the Benguela Upwelling (BENG), indicating that autotrophic conditions may be fuelled by local wind-induced nutrient inputs to the mixed layer. Sea Level Height Anomalies (SLHA), used as an indicator of mesoscale eddies, were negatively correlated with NCP anomalies offshore of the BENG upwelling fronts into the SATL, suggesting autotrophic conditions are driven by mesoscale features. The Agulhas bank and Brazil-Malvinas confluence regions also had a strong negative correlation between SLHA and NCP anomalies, similarly indicating that NCP is forced by mesoscale eddy generation in this region. Positive correlations between SST anomalies and the Multivariate ENSO Index (MEI) in the SATL, indicated the influence of El Niño events on the South Atlantic Ocean, however the plankton community response was less clear.

* Corresponding author at: Plymouth Marine Laboratory, Prospect Place, Plymouth PL1 3DH, UK.
E-mail address: dfo@pml.ac.uk (D. Ford).

https://doi.org/10.1016/j.rse.2021.112435
Received 9 July 2020; Received in revised form 27 March 2021; Accepted 2 April 2021
Available online 28 April 2021

1. Introduction

Autotrophic plankton produce up to 50% of the net organic carbon on our planet (Field et al., 1998), as they draw down carbon dioxide (CO_2) from the atmosphere into the ocean. A proportion of this NPP is respired by heterotrophic plankton, which results in a re-release of some of the fixed CO_2 back into the atmosphere. The balance between autotrophic production and heterotrophic respiration determines NCP. Measurements of NCP made on research ships, though essential to understanding the dynamics of NCP, provides only a snapshot of the system rather than broader temporal-spatial dynamics. Such measurements can be estimated by ocean colour from space (Tilstone et al., 2015a). The use of *in situ* data to identify the most accurate ocean colour satellite algorithms, will facilitate the generation of reliable synoptic-scale NCP time series. Such data are needed for identify trends in the metabolic balance of the oceans, and understand the biological draw down and release of CO_2 from the oceans.

The estimation of NCP from satellite ocean colour is dependent on the accurate quantification of NPP, which is derived from Chl *a*, photophysiological parameters (*e.g.*: maximum photosynthetic rate, P^B_m; initial slope of the light-dependent photosynthetic rate, α^B), and photosynthetically active radiation (PAR), and the estimation of the relationship between NPP and heterotrophic respiration from proxy parameters such as SST. Chl *a*, as the dominant pigment in phytoplankton, has been routinely monitored on a global scale using satellite data since the launch of the National Aeronautics and Space Administration (NASA) Sea Viewing Wide Field of View Sensor (SeaWiFS) on the Orbview-2 satellite in 1997. Following the success of SeaWiFS, MODIS-A was launched in 2002 providing continued monitoring of Chl *a* globally. Concerted efforts over the last three decades to estimate NPP from Chl *a* on a global scale resulted in the development of 20 models that use a variety of algorithm architecture (Carr et al., 2006; Friedrichs et al., 2009). A series of inter-comparisons performed by NASA indicated that NPP models of different complexities performed similarly (Friedrichs et al., 2009), though they displayed regional dependencies (Campbell et al., 2002). These inter-comparisons also highlighted that up to 50% of model uncertainties could be attributed to uncertainty in the input parameters, with by far the largest contribution coming from Chl *a* (Saba et al., 2011). Such differences in algorithm performance highlight the need to identify the best performing NPP and Chl *a* algorithms regionally, to reduce the uncertainty attributed to input parameters.

Recently NCP has been estimated from ocean colour data using empirical or semi-analytical algorithms based on NPP (Chang et al., 2014; Li and Cassar, 2016; Serret et al., 2009; Tilstone et al., 2015a). Regional empirical NCP algorithms for the Atlantic Ocean have been derived from *in vitro* ^{14}C-based NPP and O_2-based NCP estimates (Serret et al., 2009; Tilstone et al., 2015a). However, these empirical algorithms assume a spatially homogenous relationship between photosynthesis and respiration that has been shown to be variable, for example between the North and South Atlantic Oceans (Serret et al., 2015). This reinforces the need to identify the most accurate algorithms for a particular geographical region.

According to Saba et al. (2011), 22% of the uncertainty in NPP models could be attributed to the *in situ* NPP measurements uncertainty. Chl *a*, NPP and NCP algorithms will all have uncertainties in both the algorithm input parameters, and the uncertainty of the *in situ* measurements that are used to assess their performance. Previous statistical assessments have assumed that all uncertainty resides in the satellite retrievals, and consider the *in situ* measurements to be truth (*i.e.* '100% accurate'). Neglecting the *in situ* uncertainty could result in a reduction in algorithm performance, especially when limited *in situ* data exist to either calibrate or validate the algorithms.

The South Atlantic Ocean is under sampled and few *in situ* datasets are available. It is however an exceptionally dynamic and varied system, that includes the seasonal Equatorial upwelling, high productivity on the southwestern (Dogliotti et al., 2014; Garcia et al., 2004) and the southeastern shelf (Hutchings et al., 2009; Lamont et al., 2018), as well as the propagation of Agulhas Current eddies through the basin (Guerra et al., 2018). NCP variability can feasibly be observed using ocean colour remote sensing, to assess principal environmental drivers, assuming the performance of ocean colour algorithms have been evaluated. There are few studies however, that have assessed the performance of ocean colour satellite algorithms in the South Atlantic Ocean. These have been focused mainly on the southwestern shelf and Brazilian Coast, but with conflicting results (Dogliotti et al., 2014; Dogliotti et al., 2009; Garcia et al., 2005; Kampel et al., 2009b; Kampel et al., 2009a). Dogliotti et al. (2014; 2009) showed that the MODIS-A OC3M, underestimates Chl *a* on the southwestern shelf, over a range of *in situ* values spanning 0.1 to 11 mg m^{-3}. By contrast, Kampel et al. (2009b) showed that OC3M overestimates Chl *a* on the Brazilian Coast, but over a much smaller range of *in situ* values from 0.08 to 0.20 mg m^{-3}.

The objectives of this paper are to investigate the NCP dynamics in the South Atlantic Ocean, using MODIS-A multi-spectral observations, in order to assess the principal environmental drivers of NCP over a 16 year period. In order to generate accurate satellite NCP time series, the performance of MODIS-A estimates of Chl *a*, NPP and NCP for the South Atlantic Ocean are assessed, whilst also accounting for the *in situ* uncertainty. Weighted statistics are computed to account for the uncertainty in both the satellite and *in situ* data to evaluate algorithm performance. Following selection of the most accurate algorithms, a perturbation analysis to determine the magnitude of the uncertainty induced on satellite NCP by each input parameter, and on the *in situ* measurements themselves was conducted. The uncertainty analysis identifies where future efforts should focus on reducing the uncertainties in these parameters.

2. Methods

2.1. Chlorophyll-a

Chl *a* was measured semi-autonomously and continuously along seven Atlantic Meridional Transects (AMT; data available from BODC; https://www.bodc.ac.uk/) from 2009 to 2018 (Fig. 1a). Chl *a* was derived from total particulate absorption coefficients, measured using a WetLabs AC-S connected to the ships clean flow through system, which sampled the surface seawater continuously from a depth of approximately 5 m. Further details of this method are given in Brewin et al. (2016) following methods of Dall'Olmo et al. (2009), Slade et al. (2010) and Dall'Olmo et al. (2012). The AC-S Chl *a* method provided ~80,000 measurements in the study area. The *in situ* uncertainty (εins_{CHL}) in the measurements were assessed using the $\log_{10}$ root mean square difference between the HPLC Chl *a* and AC-S estimated Chl *a* for each cruise, ranging from 0.06 to 0.26 $\log_{10}$(mg m^{-3}).

A further 211 discrete Chl *a* measurements were collected along the South American coast (BRAZIL dataset) on six cruises between 2012 and 2018. For each measurement, between 0.5 and 1 L of seawater was filtered onto 25 mm GF/F filters and stored in liquid nitrogen until analysis in the laboratory. Chl *a* was extracted in a solution of acetone and di-methyl sulphoxide (DMSO) and estimated fluorometrically following the method of Welschmeyer (1994) on a 10 AU Turner Fluorometer. No replicate measurements were taken to assess the uncertainty of these values.

Additionally, 223 discrete Chl *a* measurements were collected in the South Atlantic (November 2003), Benguela upwelling system (October 2002, May 2014 and September 2014) and the Atlantic sector of the Southern Ocean (January–February 2009) on five cruises (BEN dataset). For these samples, between 1.5 and 2.4 L of seawater was filtered onto 25 mm GF/F filters and the filters were stored in liquid nitrogen until analysis ashore. Frozen filters were added to 90% acetone to extract pigments for analysis using the reverse-phase HPLC procedures outlined by Barlow et al. (1997) or Zapata et al. (2000). No replicate measurements were taken to assess the uncertainty for these estimates.

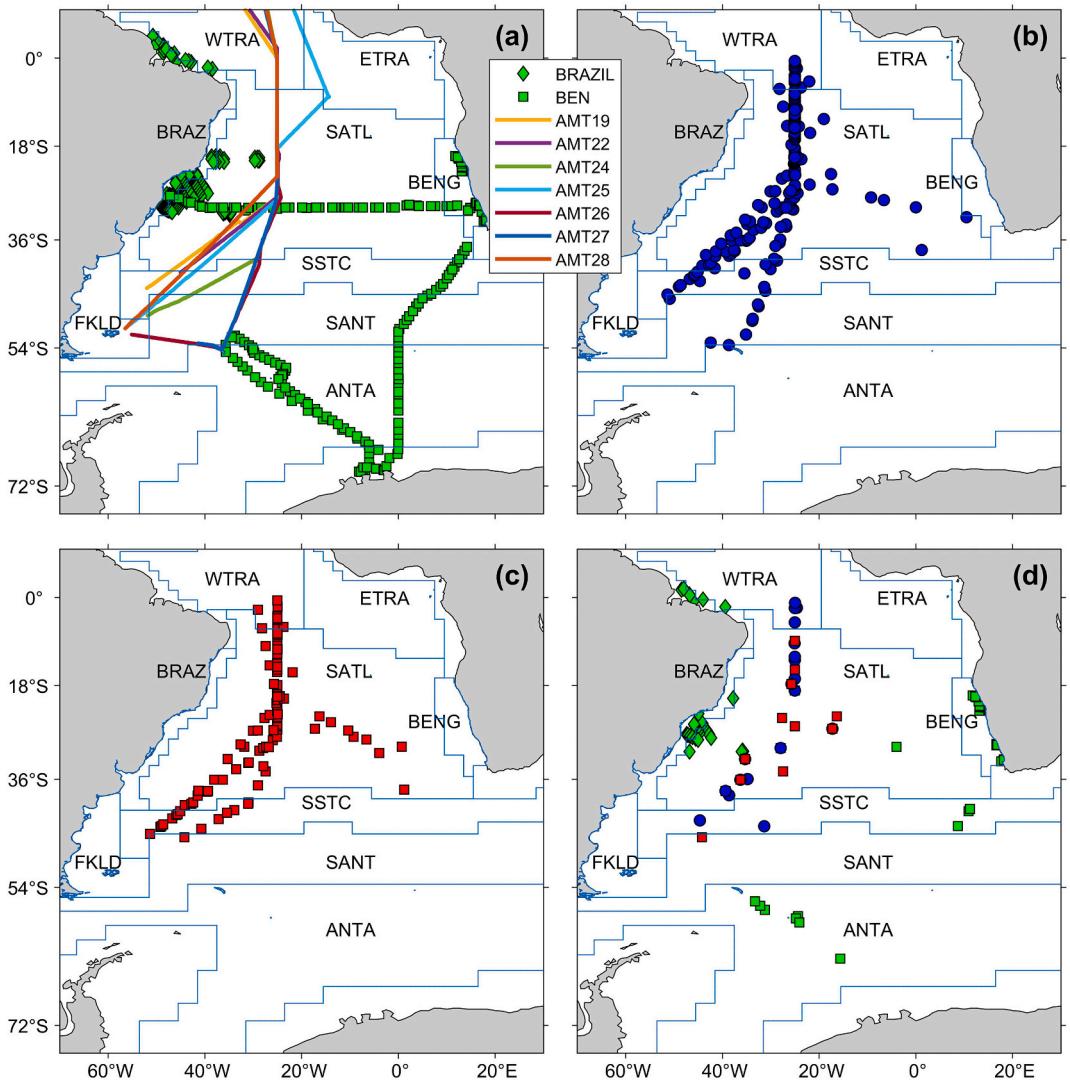

Fig. 1. Sampling locations for measurements of (a.) *in situ* chlorophyll *a* (Chl *a*) collected at discrete stations along the Brazilian coast (BRAZIL dataset, green diamonds), Benguela and Southern Ocean (BEN dataset, green squares) and continuous underway estimates collected on seven Atlantic Meridional Transect (AMT) cruises (coloured lines); (b.) *in vitro* net primary production and (c.) *in vitro* net community production both determined at discrete stations on AMT cruises between 2002 and 2019. (d) indicates discrete Chl *a* (green squares; green diamonds), net primary production (blue circles) and net community production (red squares) stations with satellite matchups. The province areas are from Longhurst (1998) as follows: WTRA is Western Tropical Atlantic; ETRA is Eastern Tropical Atlantic; BRAZ is Brazilian Current coastal; SATL is South Atlantic Gyre; BENG is Benguela Current coastal upwelling; FKLD is Southwest Atlantic shelves; SSTC is South Subtropical Convergence; SANT is Sub Antarctic and ANTA is Antarctic. (For interpretation of the references to colour in this figure legend, the reader is referred to the web version of this article.)

2.2. *In vitro* NPP

In vitro ^{14}C NPP incubations were conducted at 165 stations (Fig. 1b), from 15 AMT cruises between 2002 and 2019, following the protocols outlined in Poulton et al. (2006) and Tilstone et al. (2009). The *in situ* uncertainty (Ɛins_{NPP}) was estimated by propagating the triplicate standard deviations of the discrete depth measurements, through the water column, using the same integration scheme, for each station. Ɛins_{NPP} was on average 49 mg C m^{-2} d^{-1}, and ranged between 5 and 300 mg C m^{-2} d^{-1}.

2.3. *In vitro* NCP

In vitro NCP measurements were conducted at 95 stations (Fig. 1c) on 10 AMT cruises between 2003 and 2019 using *in vitro* changes in dissolved oxygen (O_2), following the procedures described in Gist et al. (2009). The *in situ* uncertainty (Ɛins_{NCP}) was assessed by integrating the combined standard errors of the initial and light replicate bottles, at discrete depths through the water column, following the same integration scheme, for each station. Ɛins_{NCP} was on average 20 mmol O_2 m^{-2} d^{-1} and ranged between 5 and 114 mmol O_2 m^{-2} d^{-1}. The *in situ* NCP dataset contains a subset of the data present in Tilstone et al. (2015a; N = 50), alongside an additional 45 stations from four AMT cruises; AMT 22 (2012), AMT 23 (2013), AMT 24 (2014) and AMT 29 (2019).

2.4. *Chl a Algorithms*

Satellite Chl *a* was estimated using five algorithms. The OC algorithms are based on an empirical relationship between the log-transformed blue to green remote sensing reflectance (R_{rs}) ratio and the *in situ* Chl *a* concentration (O'Reilly et al., 1998). For MODIS-A, the OC3Mv6 algorithm uses the log-transformed maximum band ratio (R) from two bands, $R_{rs}(443)$ and $R_{rs}(448)$ using $R_{rs}(547)$ as the denominator as follows:

$$R = log_{10}\left(\frac{max[R_{rs}(443), R_{rs}(488)]}{R_{rs}(547)}\right) \quad (1)$$

Chl *a* was estimated according to:

$$\text{Chl } a = 10^{\left(a_0 + a_1 R + a_2 R^2 + a_3 R^3 + a_4 R^4\right)} \quad (2)$$

where $a_0 = 0.2424$, $a_1 = -2.7423$, $a_2 = 1.8017$, $a_3 = 0.0015$ and $a_4 = -1.2280$. The algorithm performs well where phytoplankton dominate the optical signal, however in coastal waters the performance decreases, where suspended sediments and coloured dissolved organic matter (CDOM), change the optical properties of the water (Morel and Prieur, 1977).

OC5 is a modification of the OC algorithm, to improve performance in areas with increased absorption by CDOM and scattering by suspended sediments. Chl *a* concentrations are estimated by a triplicate look up table (LUT) approach, using the OC maximum band ratio, normalised water leaving radiance ($nL_w(\lambda)$ at 412 and 555 nm; Gohin et al., 2002). The algorithm was developed using observations in the English Channel and Bay of Biscay, but has been shown to perform well in other areas with high CDOM and/or sediment loads (Tilstone et al., 2011, 2017).

The GSM semi analytical model (Garver and Siegel, 1997; Maritorena et al., 2002) simultaneously estimates Chl *a*, absorption by detrital and dissolved matter at 443 nm, and particle backscatter at 443 nm

$$R_{rs}(\lambda) = \left\{\sum_{i=1}^{2} g_i \left[\frac{b_{bw} + b_{bp}(\lambda_0)\left(\frac{\lambda}{\lambda_0}\right)^{-\Upsilon}}{b_{bw} + b_{bp}(\lambda_0)\left(\frac{\lambda}{\lambda_0}\right)^{-\Upsilon} + a_w(\lambda) + chla^* a^*_{ph}(\lambda) + a_{dg}(\lambda_0) exp\left[-S_{dg}(\lambda - \lambda_0)\right]}\right]^i\right\} 0.5238 \quad (3)$$

using non-linear optimisation of the R_{rs} spectrum. The underlying bio-optical model is:

where $\lambda_0 = 443$, and g_i, γ, S_{dg} and $a^*_{ph}(\lambda)$ are predefined values (Maritorena et al., 2002) and 0.5238 is a conversion from below water to above water R_{rs}. The GSM has the advantage of solving for multiple parameters simultaneously.

The Colour Index (CI) method was developed for the clearest waters (Hu et al., 2012) to reduce impacts from artefacts and biases due to residual glint, stray light, and atmospheric correction errors in the R_{rs} spectra. A three band reflectance difference method was used between $R_{rs}(555)$ and a linear baseline between $R_{rs}(443)$ and $R_{rs}(670)$. For MODIS-A, the associated bands are band shifted to those required by the CI. The approach is merged with the OC algorithm (OCI) in the standard NASA Chl *a* algorithm to improve retrievals in the oligotrophic gyres (Hu et al., 2012). For this work, the CI was merged with OC3 and OC5 (OC3-CI and OC5-CI) blending linearly between 0.15 and 0.2 mg m^{-3}.

2.5. NPP Algorithms

NPP was determined using three algorithms, which have previously shown to be accurate regionally in the Atlantic Ocean and/or the South Atlantic Ocean (Campbell et al., 2002; Carr et al., 2006; Dogliotti et al., 2014; Friedrichs et al., 2009; Lobanova et al., 2018; Tilstone et al., 2015b; Tilstone et al., 2009). In each case, satellite Chl *a* determined by the best performing algorithm was used as input. The Vertical Generalized Production Model (VGPM; Behrenfeld and Falkowski, 1997) estimates NPP in the euphotic zone (1% light level) taking the form:

$$NPP_{VGPM} = Chla\ z_{eu}\ 0.66125 \left[P^B_{opt}\frac{I_0}{4.1 + I_0}\right] DL \quad (4)$$

where DL is the day length, z_{eu} is the euphotic zone depth and I_0 is the daily surface PAR. P^B_{opt} is the biomass specific optimum photosynthetic rate retrieved as a function of SST (Behrenfeld and Falkowski, 1997).

The Platt and Sathyendranath model (PSM; Platt et al., 1991) estimates daily NPP at a specific depth (z), based on an exponential photosynthetic-irradiance (P—I) function (square brackets):

$$NPP(z)_{PSM} = Chla(z)\left[P^B_m\left(1 - exp\left(-\frac{\alpha^B I(z)}{P^B_m}\right)\right)\right] DL \quad (5)$$

where, I(z) is PAR at z. The P—I function is driven by two parameters: the biomass specific maximum photosynthetic rate (P^B_m) and the initial slope of the light-dependent photosynthetic rate (α^B). These parameters cannot be determined using remote sensing, therefore *in situ* values were used from a published database (Bouman et al., 2018) averaged across the provinces (Fig. 1) and seasons in which the *in situ* NPP were sampled; $P^B_m = 3.43$ mg C (mg Chl)$^{-1}$ h^{-1} and $\alpha^B = 0.039$ mg C (mg Chl)$^{-1}$ h^{-1} (μEm^{-2} s^{-1})$^{-1}$. $NPP(z)_{PSM}$ was integrated to z_{eu} to provide total water column NPP_{PSM} (Lobanova et al., 2018).

The P—I function was propagated through the water column using the Beer-Lambert-Bouguer law, as a function of surface PAR (I_0):

$$I(z) = I_0 exp(-K_d z) \quad (6)$$

where K_d is the downwelling diffuse attenuation coefficient of PAR. Z_{eu} for the VGPM and PSM was estimated using the following equation, derived from Eq. (6), assuming I_0 is 100% of the surface PAR and PAR at the euphotic zone depth is 1%:

$$z_{eu} = -\frac{ln(0.01)}{K_d} = \frac{4.6}{K_d} \quad (7)$$

where K_d for the PAR spectrum was calculated as a function of K_d at 490 nm (Morel et al., 2007) available from satellite estimates (see Section 2.7 for data source). The PSM was therefore run as a broad-band model using PAR as the input light parameter.

The Wavelength Resolved Model (WRM) of Morel (1991), implemented following Smyth et al. (2005), spectrally resolves the irradiance and associated phytoplankton response. The WRM takes the form:

$$NPP_{WRM} = 12\ a^*_{max}\phi_m \int_0^{DL}\int_0^{z_{eu}}\int_{400}^{700} Chl\ a(z)\ PUR\ (z,t,\lambda)\ f(x(z,t))\ d\lambda\ dz\ dt \quad (8)$$

where, a^*_{max} is the maximum phytoplankton Chl *a* specific absorption coefficient and Φ_m is the maximum quantum yield for growth, both parametrised using Chl *a* following Morel et al. (1996), and PUR is the phytoplankton usable radiation. The PSM can also be run in a wavelength resolving configuration. The above-water incident PAR was computed from the Gregg and Carder (1990) model at 5 nm wavelength and 1 min time resolution. Meteorological and ozone data were obtained from the National Centres for Environmental Prediction (NCEP) and Earth Total Ozone Mapping Spectrometer data (EPTOMS), respectively. Cloud cover fields were obtained from the European Centre for Medium Range Weather Forecasts (ECMWF) ERA5 model reanalysis product, downloaded from the Copernicus Climate Data Store (CCDS; https://cds.climate.copernicus.eu/), and used to modify the light field following Reed (1977). NPP_{WRM} was integrated to the same z_{eu} as the VGPM and

PSM, computed using Eq. (7).

2.6. NCP Algorithms

NCP was estimated using four empirical algorithms as described in Tilstone et al. (2015a). All four algorithms are based on a power law relationship between NPP and NCP. NCP-A was derived using data from mainly net heterotrophic areas of the North Atlantic Ocean (negative NCP). NCP-B was derived using data from mainly net autotrophic areas of the North Atlantic Ocean (positive NCP; Serret et al., 2009). These algorithms take the form:

$$NCP_A = 49.53^* \int {}^{14}CNPP^{0.48} - 300 \text{ (AMT6 Model)} \quad (9)$$

$$NCP_B = 212.01^* \int {}^{14}CNPP^{0.15} - 300 \text{ (AMT11 Model)} \quad (10)$$

Two further algorithms, NCP-C and NCP-D, were developed using data spanning net autotrophic and net heterotrophic regimes in the Atlantic Ocean, but weighted towards the North Atlantic Ocean. An additional relationship between NCP and SST is included in the NPP exponent for NCP-D (Tilstone et al., 2015a):

$$NCP_C = 163.83^* \int {}^{14}CNPP^{0.2035} - 300 \quad (11)$$

$$NCP_D = 179.86^* \int {}^{14}CNPP^{(0.2487+(-0.0036^*SST))} - 300 \quad (12)$$

2.7. MODIS-A data

MODIS-A Level 1 images downloaded from the NASA Ocean Colour website (https://oceancolor.gsfc.nasa.gov) were processed to Level 2 (Reprocessing 2018) 1 km products using SeaDAS v7.5 using the standard atmospheric correction and projected onto a linearly spaced 1 km grid for matchup analysis. PAR, $K_d(490)$ and SST were processed alongside Chl *a* using standard MODIS-A algorithms, as described on the NASA Ocean Colour website (https://oceancolor.gsfc.nasa.gov/atbd/), as inputs to the NPP and NCP algorithms. The AMT, BEN and BRAZ Chl *a* datasets used 56, 38 and 30 images respectively for matchup analysis.

The procedure for matchup analysis described in Brewin et al. (2016) was followed using level 2, 1 km products. Although Brewin et al. (2016) highlighted that level 3, 4 km products could be used to evaluate the continuously measured AMT Chl *a* dataset, NPP and NCP *in situ* measurements represent discrete water samples, driving the choice of level 2, 1 km products. Discrete station data were subjected to the same quality checks (Brewin et al., 2016), including the elimination of data collected at night, leading to an approximate time window of ±8 h, to remain consistent between continuous and discrete datasets. A 3 × 3 pixel window centred on each 1 km station-matchup pixel was selected to test for spatial homogeneity, and matchups with fewer than 5 valid pixels within the 3 × 3 pixel windows (after standard L2 flags were applied), were excluded from further analysis (Bailey and Werdell, 2006).

After selection of the most accurate algorithms, MODIS-A monthly 4 km Chl *a* composites were produced for the entire South Atlantic domain using OC3-CI. Monthly composites of NPP were computed with the WRM using the LUT described in Smyth et al. (2005), using additional input composites of MODIS-A PAR, $K_d(490)$ and SST downloaded from the NASA Ocean Colour website (https://oceancolor.gsfc.nasa.gov/l3/). Monthly NCP composites were assembled using NCP-D, to perform a monthly time series analysis against climate indices and environmental drivers between July 2002 and December 2018. Monthly NCP anomalies were calculated on a per pixel basis, by subtracting from the monthly NCP the corresponding month's climatological NCP value computed using a time series between 2002 and 2018.

Table 1
Tabulated algorithm uncertainties (Ɛa) used for parameterisation with *in situ* data from the literature.

Algorithm	Algorithm uncertainty (Ɛa)	Reference
Chl *a* Algorithms		
Uncertainty units: $\log_{10}$(mg m^{-3})		
OC3 + OC3CI[a]	0.255	NASA Oceancolour Website
GSM	0.156	(Maritorena et al., 2002)
OC5 + OC5CI[a]	0.220	(Gohin et al., 2002)
NPP Algorithms		
Uncertainty units: $\log_{10}$(mg C m^{-2} d^{-1})		
VGPM	0.24	(Friedrichs et al., 2009)
PSM	0.24[b]	N/A
WRM	0.16	(Smyth et al., 2005)
NCP Algorithms		
Uncertainty units: mmol O_2 m^{-2} d^{-1}		
NCP-A	103	(Tilstone et al., 2015a)
NCP-B	46	(Tilstone et al., 2015a)
NCP-C	40	(Tilstone et al., 2015a)
NCP-D	35	(Tilstone et al., 2015a)

[a] Indicates for OC3-CI and OC5-CI the uncertainty is assumed to be the same as the non-CI version.
[b] Indicates for the PSM an uncertainty value to our knowledge is unavailable, and therefore assume the same value as the VGPM.

2.8. Uncertainties in satellite data

The combined uncertainty in the satellite measurements ($ƐC_{ALGORITHM}$) was estimated as the combination of three components (BIPM, 2008). Firstly, the stated uncertainty of the algorithm ($Ɛa_{ALGORITHM}$) during the parameterisation with *in situ* data was taken from the literature (see Table 1). Secondly, the spatial uncertainty in the satellite data ($Ɛs_{ALGORITHM}$) were estimated using the standard deviation of the 3 × 3 pixel grid used to test for homogeneity. Finally, the uncertainty attributed to the satellite input parameters ($Ɛi_{ALGORITHM}$) was calculated as follows: For NPP and NCP algorithms Ɛi was estimated using a Monte Carlo uncertainty propagation, where 1000 calculations were made perturbing the input products using random noise representing the uncertainty on the MODIS-A retrieval of each parameter ($ƐR_{PARAMETER}$). For Chl *a*, Ɛi is normally calculated from the uncertainty in Rrs, but this is outside the scope of this work. ƐR for Chl *a* and NPP were assessed in this paper as $\log_{10}$ root mean square difference (log-RMS) values. ƐR for SST was taken as the RMS value of a comparison of MODIS-A SST to *in situ* skin SST (details in Appendix 3; Table A7). ƐR for PAR and $K_d(490)$ were estimated using SeaWiFS Bio-optical Archive and Storage System (SeaBASS) matchups between *in situ* and MODIS-A data from a global dataset (PAR ƐR = 5.6 Einstein m^{-2} d^{-1}, and $K_d(490)$ ƐR = 0.257 in $\log_{10}$ space).

The three components (Ɛa, Ɛs and Ɛi) are assumed to be independent, and combined in quadrature (Taylor, 1997) to estimate $ƐC_{ALGORITHM}$ for each matchup:

$$ƐC = \sqrt{Ɛa^2 + Ɛs^2 + Ɛi^2} \quad (15)$$

2.9. Weighted statistical analyses

Measured and satellite estimates of each parameter were compared in $\log_{10}$ space. To enable $\log_{10}$ transformation of NCP estimates, the minimum value of the satellite matchups (−170 mmol O_2 m^{-2} d^{-1}) was added to each value.

The measured and satellite estimates were first evaluated using a non-weighted statistical approach to assess the performance of satellite

algorithms (e.g: Brewin et al., 2015; Dogliotti et al., 2014; Dogliotti et al., 2009). A Type-II regression analysis was employed to calculate the slope, intercept and the percentage variability explained by the linear regression (R^2). To evaluate the accuracy of each model, the absolute percentage difference (APD), log-RMS and the mean (M) and standard deviation (S) of the $\log_{10}$ difference were calculated. Following the methods of Campbell et al. (2002) the inverse $\log_{10}$ difference between the *in situ* and satellite values of 10^{M} (F_{med}), 10^{M+S} (F_{max}) and 10^{M-S} (F_{min}) were calculated. The number of matchups used to compute the statistics (N) is also given.

The estimates were then evaluated by a weighted statistical approach using weighted variants of the previously mentioned statistics. The weights for each matchup were computed using Ɛins and ƐC:

$$weight = \frac{1}{\sqrt{Ɛins^2 + ƐC^2}} \tag{16}$$

The weights were rescaled between zero and one. This approach allows the satellite and *in situ* uncertainties to be accounted for in the statistical analysis, which was not previously possible, because *in situ* data uncertainties were not determined. The approach emphasises matchups where both the satellite and *in situ* measurements are more certain, while less certain matchups produce a smaller effect on the overall statistics. For the BRAZIL and BEN datasets, no *in situ* uncertainty could be calculated, and therefore the weighting uses only the satellite uncertainty (Appendix 2). NCP algorithms were assessed firstly driven using *in situ* NPP and *in situ* SST, and secondly driven by MODIS-A estimates.

2.10. Uncertainty perturbation analysis

Following the methods of Saba et al. (2011), a perturbation analysis was conducted to determine the potential reduction in NCP-D log-RMS which could be attributed to uncertainties in the satellite input parameters and *in situ* NCP. This analysis quantifies the range of uncertainty introduced in satellite NCP estimates from the input parameters, including the *in situ* NCP used to validate these estimates. Each of the input parameters; Chl *a*, PAR and SST can have three possible values for each NCP measurement (original value, original – ƐR and original + ƐR). The WRM algorithm used to determine NPP also has an uncertainty (log-RMS found in this paper, using weighted statistics: 0.20; Table 3), and therefore three values are also possible. For each NCP measurement, 81 perturbations of the input data were calculated. Similarly, each *in situ* NCP measurement could also have three perturbations (original value, original - $Ɛins_{NCP}$, original + $Ɛins_{NCP}$). Log-RMS was used to assess the performance of NCP-D under different scenarios. For each NCP measurement, the 81 perturbations were examined and the perturbation that produced the lowest log-RMS from 4 scenarios was selected, in order to assess the potential reduction in log-RMS that could be attributed to each of the parameters. The 4 scenarios tested were: (1) uncertainty in individual input parameters (Chl *a*, PAR, SST and NPP algorithm), (2) uncertainty in all input parameters together, (3) uncertainty in *in situ* NCP measurements and (4) uncertainty in all input parameters *and in situ* NCP. The analysis focused on the reduction in log-RMS, however considering the uncertainties from the input parameters could also increase log-RMS. The input parameter uncertainties that have the greatest control on satellite NCP uncertainties were therefore indicated.

2.11. Climate indices and environmental drivers

Climate indices indicate large-scale variability in physical parameters in the ocean. Satellite estimated NCP anomalies were compared to three climate indices: the North Atlantic Oscillation (NAO), indicating atmospheric pressure conditions in the North Atlantic, downloaded from http://www.cgd.ucar.edu/cas/catalog/; the Multivariate ENSO Index (MEI) as an indicator of El Niño Southern Oscillation (ENSO) phases, downloaded from https://www.esrl.noaa.gov/psd/enso/mei and the Southern Annular Mode (SAM), indicating the displacement of the westerly winds in the Southern Ocean, downloaded from http://www.nerc-bas.ac.uk/icd/gjma/sam.html.

Changes in wind forcing can affect the distribution of phytoplankton through changes in the mixed layer. ECMWF ERA5 monthly wind speeds were downloaded from the CCDS (https://cds.climate.copernicus.eu/), with a resolution of 0.25°, coincident with the MODIS-A NCP time series (July 2002 – December 2018). Wind speed anomalies were calculated by subtracting from the monthly wind speed, the corresponding monthly climatology value calculated from the ECMWF ERA5 wind speed.

Sea Level Height Anomalies (SLHA) can be associated with mesoscale processes and water mass changes, which can contribute to changes in phytoplankton distributions across basins. Monthly mean SLHA were downloaded from AVISO+ (https://www.aviso.altimetry.fr/) coinciding with the MODIS-A NCP time series at a resolution of 0.25°. Anomalies were calculated by AVISO+ with respect to a 25 year climatology between 1993 and 2018.

2.12. Time series analysis

Mean monthly NCP anomalies were averaged from 4 km monthly NCP anomaly maps for the South Atlantic Longhurst provinces; WTRA, ETRA, SATL, BRAZ, BENG, FKLD and SSTC (Fig. 1; Longhurst, 1998). The potential drivers of NCP variability were explored firstly by calculating Spearman correlation coefficients between monthly province-averaged NCP anomalies, climate indices and environmental drivers. The use of anomalies to determine correlations reduces the effect of temporal autocorrelation which may complicate interpretation.

Averaging NCP anomalies over the provinces may highlight the dominant drivers of variability but mask the effects of opposing trends within a province as well as the more subtle and localised drivers, such as mesoscale eddies. The localised forcing is explored using a per pixel correlation approach, where a monthly time series of NCP anomalies is generated for each 4 km pixel for comparison against environmental drivers (Spearman correlation, $\alpha = 0.05$). Spatial autocorrelation was tested using the method of field significance (Wilks, 2006).

The uncertainties in NCP anomalies were propagated through the Spearman correlations using a Monte Carlo uncertainty propagation. Each monthly NCP measurement in the time series, was perturbed with random noise representing the uncertainty of the MODIS-A NCP estimate 1000 times as in Section 2.8, and the Spearman correlations were repeated. The 95% confidence interval was calculated from the resulting distribution of the correlations. The correlation was deemed significant ($\alpha = 0.05$), where the 95% confidence interval remained significant. The per pixel analysis was repeated for NPP and SST anomalies.

3. Results

3.1. Accuracy assessment of MODIS-A Chl a

Weighted regression analysis between *in situ* Chl *a* and five MODIS-A algorithms for data collected on seven AMT campaigns is given in Fig. 2, and the associated statistical analysis are given in Table 2. Using the weighted approach to determine the algorithm performance, all five algorithms performed similarly, with $R^2 > 0.9$ and log-RMS < 0.20. OC3-CI, the standard MODIS-A algorithm, showed the best performance with the lowest log-RMS, slope close to 1 and F_{min}, F_{med} and F_{max} close to

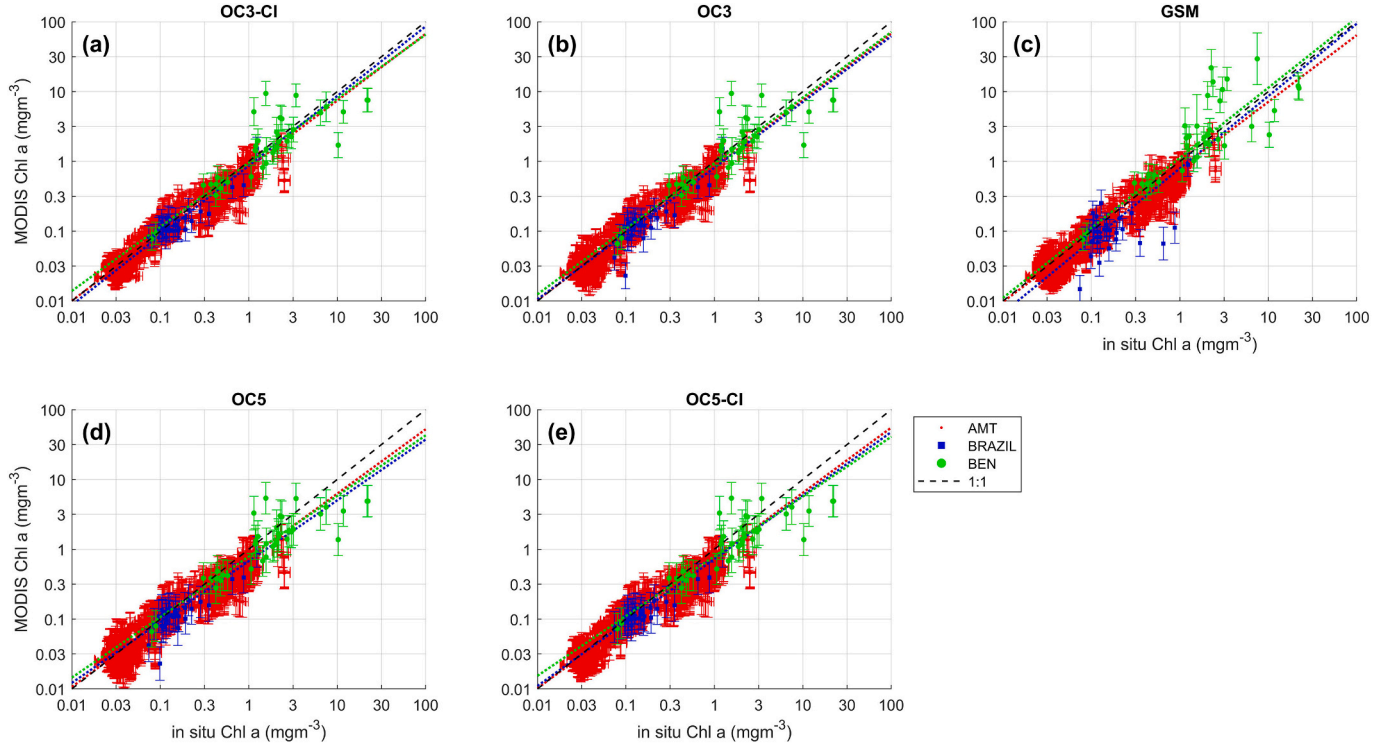

Fig. 2. Comparison of *in situ* and MODIS-A estimates of chlorophyll *a* for: (a) OC3-CI, (b) OC3, (c) GSM, (d) OC5 and (e) OC5-CI. Algorithms are described in Section 2.3. Red points indicate satellite matchups with the continuous Atlantic Meridional Transect (AMT) dataset, blue squares the Brazilian dataset (BRAZIL) and green squares the Benguela dataset (BEN). Black dashed line is 1:1 line, red dashed line is a weighted Type-II linear regression for the AMT dataset, blue dashed line is a weighted Type-II linear regression for the Brazilian dataset and green dashed line the weighted Type-II linear regression for the Benguela dataset. Horizontal error bars indicate *in situ* uncertainty ($\mathcal{E}ins_{CHLA}$). Vertical error bars indicate the combined satellite uncertainty ($\mathcal{E}C$). (For interpretation of the references to colour in this figure legend, the reader is referred to the web version of this article.)

Table 2
Performance indices for satellite chlorophyll *a* algorithms using the AMT dataset. Log-differences uncertainties in satellite estimates are mean (M), standard deviation (S) and Root Mean Square (log-RMS).

Weighted (All)												
AMT	Model	R^2	Slope	Intercept	log-RMS	APD	M	S	F_{min}	F_{med}	F_{max}	N
	OC3-CI	**0.93**	**0.96**	**−0.08**	**0.16**	**123**	**0.06**	**0.14**	0.83	1.16	**1.61**	1440
	OC3	0.91	**0.96**	**−0.08**	**0.17**	**122**	**0.05**	0.16	0.78	**1.13**	1.65	1440
	GSM	0.91	**0.96**	**−0.10**	0.18	144	0.09	0.16	0.84	1.22	1.77	1440
	OC5	0.91	0.92	−0.13	0.19	166	0.08	0.17	0.82	1.21	1.79	1440
	OC5-CI	**0.93**	0.93	−0.12	0.18	163	0.09	**0.15**	**0.87**	1.23	1.74	1440
Weighted (Chl < 0.15 mg m^{-3})												
AMT	OC3-CI	**0.87**	**1.05**	0.04	**0.10**	**6.9**	**0.01**	**0.10**	**0.81**	1.03	**1.30**	884
	OC3	0.74	1.05	0.06	0.14	9.4	**0.00**	0.14	0.72	**1.00**	1.40	884
	GSM	0.72	1.02	**0.00**	0.14	9.5	0.03	0.14	0.79	1.08	1.48	884
	OC5	0.74	1.04	0.03	0.14	8.6	**0.01**	0.14	0.75	**1.02**	1.40	884
	OC5-CI	**0.87**	**1.05**	0.04	**0.10**	**7.0**	**0.02**	**0.10**	**0.83**	1.05	**1.33**	884

The mean and one sigma range of the difference are given as; F_{med}, F_{min} and F_{max}; values closer to 1 indicate greater accuracy. APD is the Absolute Percentage Difference. N indicates the number of matchups used to compute statistics. The most accurate algorithm for each statistic is highlighted in bold. Statistics were computed by weighting each station based on the *in situ* and satellite uncertainty (weighted). The statistics were performed on firstly, all the available matchups, and secondly, on matchups where *in situ* Chl *a* < 0.15 mg m^{-3}.

1. All algorithms had positive M indicating a tendency to underestimate Chl *a*. OC5-CI, GSM and OC5 were characterised by higher values of M compared to OC3-CI and OC3, and by F_{med} and F_{max} values greater than 1, highlighting that these three algorithms perform worse compared to OC3-CI and OC3 at the medium and maximum range Chl *a* values (Table 2). OC3-CI and OC5-CI showed lower scatter at Chl *a* < 0.15 mg m^{-3} (Fig. 2a, e), compared to OC3 and OC5 (Fig. 2b, d), which resulted in a lower S over this range (Table 2).

For both the BEN and BRAZIL datasets the weighting used only the satellite uncertainty. For the BEN, the trend in MODIS-A Chl *a* algorithms was similar to that of the AMT dataset except for the GSM (Appendix 2 Table A6), which had a higher log-RMS, higher S and negative M and a tendency to overestimate Chl *a* above 3 mg m^{-3} (Fig. 2c). For the BRAZIL dataset, the trends were different (Appendix 2 Table A5); the GSM exhibited the worst performance with lowest R^2, highest log-RMS, M and S, indicating a failure in the algorithm to estimate Chl *a* accurately in this region (Fig. 2c).

3.2. Accuracy assessment of MODIS-A NPP

There was a high variability in the *in situ* NPP uncertainty at each station. This was accounted for using the weighted method, which then

Table 3
Performance indices for satellite net primary production algorithms. Log-differences uncertainties in satellite estimates are mean (M), standard deviation (S) and Root Mean Square (log-RMS).

Weighted											
Model	R^2	Slope	Intercept	Log-RMS	APD	M	S	F_{min}	F_{med}	F_{max}	N
VGPM	0.72	**0.97**	0.06	**0.22**	**6.9**	**0.00**	0.22	0.61	**1.01**	**1.68**	18
PSM	**0.79**	0.88	0.05	0.32	9.6	0.25	0.20	**1.11**	1.77	2.82	18
WRM	**0.81**	**0.96**	**0.02**	**0.20**	**6.3**	0.07	**0.18**	0.78	1.18	1.79	18

The mean and one sigma range of the difference are given as; F_{med}, F_{min} and F_{max}; values closer to 1 indicate greater accuracy. APD is the Absolute Percentage Difference. N indicates the number of matchups used to compute statistics. The most accurate algorithm for each statistic is highlighted in bold. Statistics were computed by weighting each station based on the *in situ* and satellite uncertainty (weighted).

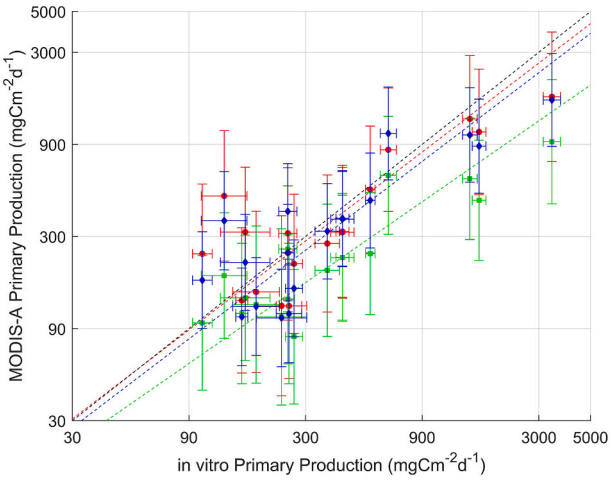

Fig. 3. Comparison of *in vitro* and MODIS-A estimated net primary production. Algorithms are described in Section 2.5. Black dashed line is the 1:1 line. Dashed lines indicate weighted Type-II line regression for the VGPM (red), PSM (green) and WRM (blue). Horizontal error bars indicate *in situ* uncertainty ($\mathcal{E}ins_{PP}$). Vertical error bars indicate the combined satellite uncertainty ($\mathcal{E}C$). (For interpretation of the references to colour in this figure legend, the reader is referred to the web version of this article.)

showed that the WRM exhibited the best performance (Table 3, Fig. 3) with the lowest log-RMS, slope closest to 1 and intercept closest to 0. The VGPM also had low log-RMS and M equal to 0 but displayed the lowest R^2 and the highest S (Table 3). The PSM had high R^2 but systematically underestimated NPP with F_{min}, F_{med} and F_{max} greater than 1.

3.3. Accuracy assessment of MODIS-A NCP

The four NCP algorithms were firstly run using *in situ* NPP and *in situ* SST ($N = 84$) to assess their accuracy (Fig. 4, Table 4). Using the weighted approach NCP-C was the most accurate, with low log-RMS and S and the highest R^2. NCP-D had a higher log-RMS and lower R^2. NCP-B tended to overestimate NCP, indicated by F_{min} and F_{med} less than 1 but had a similar log-RMS to NCP-C and NCP-D. NCP-A had the highest slope, log-RMS, M and S indicating a tendency to underestimate NCP with F_{min}, F_{med} and F_{max} all greater than 1.

MODIS-A SST and NPP using the WRM model were then applied to estimate NCP ($N = 14$; Fig. 5; Table 5). Using the weighted approach, NCP-D showed the highest R^2, low log-RMS and lowest S, and of all four algorithms was the most accurate. NCP-C showed a similar accuracy, but the slope deviated further from 1. Both algorithms tended to underestimate NCP when driven by MODIS-A NPP, compared to the *in situ* NPP. NCP-B tended to overestimate NCP, indicated by F_{min} less than 1. NCP-A tended to underestimate NCP indicated by F_{med} and F_{max} greater than 1, low R^2 and high log-RMS. Overall, NCP-D was identified as the most accurate NCP algorithm to apply to the MODIS-A time series.

3.4. Uncertainty perturbation analysis

For the scenario in which the uncertainty in both the input parameters and *in situ* NCP measurements were considered, log-RMS decreased by 87% (Table 6). The uncertainties in the NPP model (40%) and *in situ* NCP (36%) accounted for the largest reduction in log-RMS. Chl *a* uncertainties accounted for a reduction in log-RMS of 22%, whereas PAR and SST contributed the smallest reductions in the log-RMS of 2.8% and 3.5% respectively.

3.5. NCP time series analysis

Since NCP-D was the most accurate NCP algorithm, it was applied to the MODIS-A time series. There were no significant correlations between province-averaged NCP anomalies, climate indices and environmental drivers, when the uncertainties were accounted for.

On a per pixel basis and accounting for the uncertainties, there were significant correlations between NCP anomalies, with SLHA, wind speed anomalies, and the MEI (Fig. 6a, b, c). NCP anomalies were positively correlated with wind speed anomalies along the BENG coast (Fig. 6b). Negative correlations between NCP anomalies and SLHA occurred offshore in the BENG extending to the SATL (Fig. 6a). Significant negative correlations between NCP anomalies and SLHA, were also observed along the boundary between the SATL and SSTC. Positive correlations between NCP anomalies and wind speed anomalies, occurred in the SATL, especially around the centre of the South Atlantic gyre (Fig. 6b) which extended north into the WTRA. Patchy negative correlations between NCP anomalies and the MEI were observed (Fig. 6c), but were at the limits of significance (Wilks, 2006). No significant correlations were found between NCP anomalies and the NAO and SAM.

4. Discussion

4.1. Satellite uncertainty analysis

This is one of the first studies to evaluate the performance of and uncertainties in MODIS-A Chl *a*, NPP and NCP over the entire South Atlantic basin, using a comprehensive *in situ* dataset. In the following sections the reasons for the algorithms performance and where and why some of them fail is explored.

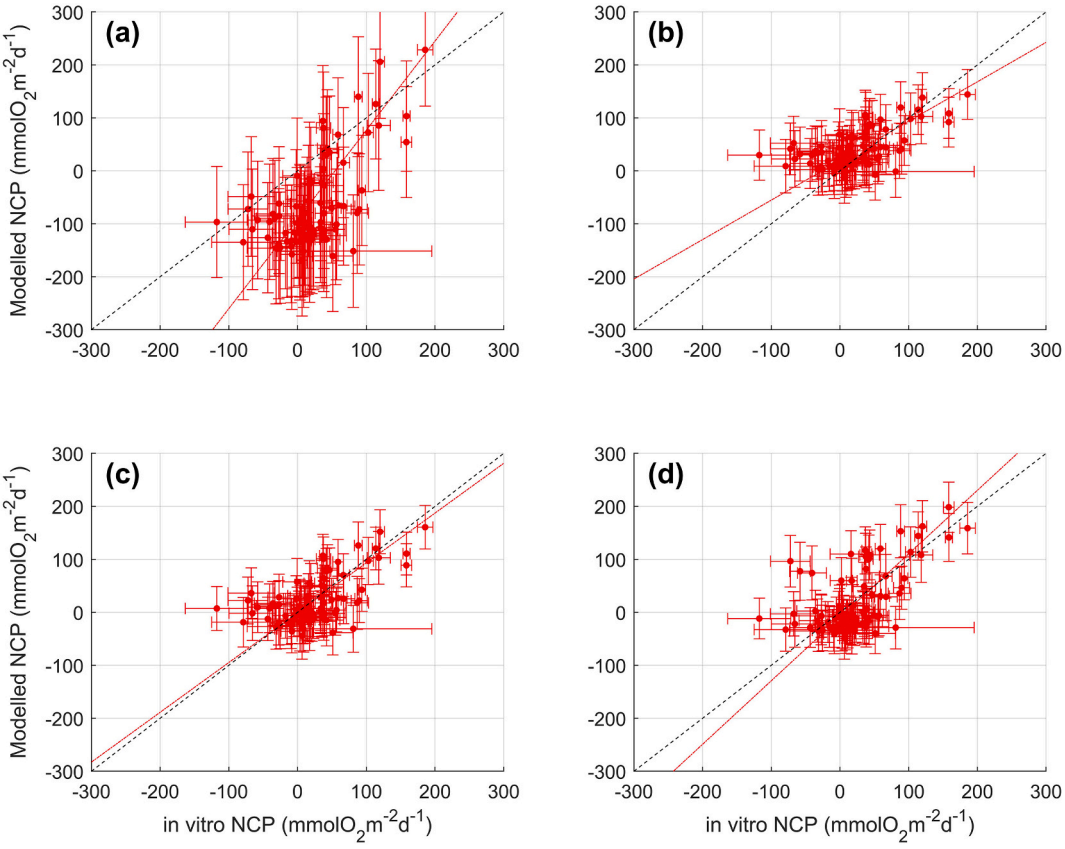

Fig. 4. Comparison of net community production (NCP) algorithms driven using *in situ* net primary production and sea surface temperature where each scatter plot refers to (a) NCP-A, (b) NCP-B, (c) NCP-C and (d) NCP-D. Algorithms are described in Section 2.6. Black dashed line is the 1:1 line. Red dashed line indicates a weighted Type-II linear regression. Horizontal error bars indicate *in situ* uncertainty ($\mathfrak{E}ins_{NCP}$). Vertical error bars indicate the *in situ* uncertainty in NPP and SST propagated through the NCP algorithms. (For interpretation of the references to colour in this figure legend, the reader is referred to the web version of this article.)

Table 4
Performance indices for net community production (NCP) algorithms driven by *in situ* net primary production and *in situ* sea surface temperature.

Weighted											
Model	R^2	Slope	Intercept	Log-RMS	APD	M	S	F_{min}	F_{med}	F_{max}	N
A	0.17	1.17	−0.68	0.53	18.11	0.39	0.36	**1.09**	2.47	5.60	84
B	**0.30**	**0.93**	0.16	**0.11**	**3.4**	−0.04	**0.10**	0.72	0.90	**1.14**	84
C	**0.31**	**0.95**	**0.09**	**0.10**	**3.5**	**0.00**	**0.10**	0.79	**1.00**	1.28	84
D	0.26	0.90	0.17	**0.12**	**4.2**	**0.02**	**0.12**	0.80	1.05	1.37	84

To log transform negative NCP values, we added the minimum value (−170 mmol O_2 $m^{-2}d^{-1}$) to all values. Log-differences uncertainties in satellite estimates are mean (M), standard deviation (S) and Root Mean Square (log-RMS). The mean and one sigma range of the difference are given as; F_{med}, F_{min} and F_{max}; values closer to 1 indicate greater accuracy. APD is the Absolute Percentage Difference. N indicates the number of matchups used to compute statistics. The most accurate algorithm for each statistic is highlighted in bold. Statistics were computed by weighting each station based on the *in situ* and satellite uncertainty (weighted).

4.1.1. Accuracy assessment of MODIS-A Chl *a*

Previous studies in this region showed that MODIS-A OC3M tends to underestimate Chl *a* on the Patagonian Shelf over a Chl *a* range of 0.2 to 6 mg m^{-3} (Dogliotti et al., 2009) and 0.3 to 11 mg m^{-3} (Dogliotti et al., 2014). Dogliotti et al. (2009) suggested that the underestimate is caused by increased aerosol loading off the Patagonian deserts, generating lower than expected R_{rs}(412) and R_{rs}(443) retrievals. Our results would suggest that this is not a local underestimation. In this study, we found that OC3-CI performed most accurately out of the five algorithms tested. There was, however, a tendency in all algorithms tested to underestimate Chl *a*, especially at concentrations >0.3 mg m^{-3} (Fig. 2).

Szeto et al. (2011) found that the Chl *a* in the Atlantic Ocean was generally overestimated, however the majority of their Atlantic data were from the North American coast. Brewin et al. (2016) showed that using the same AC-S derived Chl *a*, OC3M Chl *a* were close to the 1:1 line and had a low bias. Compared to our results this could suggest bio-optical differences between the North and South Atlantic, resulting in an underestimation that may relate to changes in CDOM to Chl *a* ratios (Szeto et al., 2011), driven by changes in the phytoplankton community structure (Organelli and Claustre, 2019).

MODIS-A is now in its 18th year of operation and has known degradation in the blue bands (412 and 443 nm; Meister and Franz, 2014). NASA have corrected for some of this and conducted a vicarious calibration for these bands; the newly reprocessed data (R2018) prove to be accurate (NASA, 2018). The OC5 algorithm uses the 412 nm band to account for atmospheric overcorrection and/or CDOM absorption. Anomalies with this band have previously been reported, associated with the performance of the GSM (Maritorena et al., 2010), and may explain why OC5 performs worse than the other algorithms tested. Differences in the reprocessing versions may account for the difference

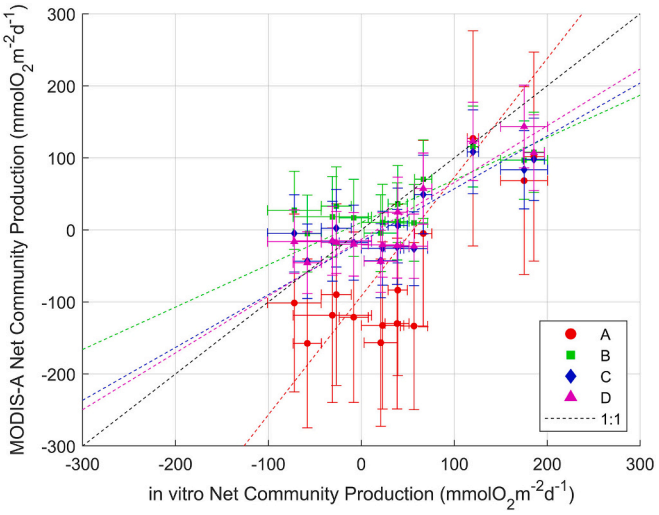

Fig. 5. Comparison of *in vitro* and MODIS-A estimated net community production (NCP). Algorithms are described in Section 2.6. Black dashed line is the 1:1 line. Red, green, blue and pink dashed lines indicate a weighted Type-II linear regression for the A, B, C and D algorithms respectively. Horizontal error bars indicate *in situ* uncertainty ($\mathrm{\mathcal{E}ins_{NCP}}$). Vertical error bars indicate the combined satellite uncertainty ($\mathrm{\mathcal{E}C}$). (For interpretation of the references to colour in this figure legend, the reader is referred to the web version of this article.)

found in this study to previous studies (Brewin et al., 2016; Dogliotti et al., 2014; Dogliotti et al., 2009; Kampel et al., 2009b). The regional bias for the South Atlantic shown in this study highlights the on-going need to monitor the performance of satellite ocean colour data, especially in regions where *in situ* data are sparse.

4.1.2. Accuracy assessment of MODIS-A NPP

Using MODIS-A OC3-CI Chl *a* as input to the NPP models, the WRM was the most accurate algorithm for this area, followed by the VGPM, similar to findings of Tilstone et al. (2009) for the entire Atlantic basin. The general trend in all three algorithms was an underestimation of NPP, especially at higher values, and reflects the trend in MODIS-A Chl *a*. Platt and Sathyendranath (1988) showed that the largest contributor to NPP variability is Chl *a*. Using *in situ* Chl *a* data, Tilstone et al. (2009) showed that the WRM and VGPM tend to overestimate NPP in the SATL during the period 1998 to 2005. This contrasts our results using MODIS-A Chl *a*, which showed an underestimate in NPP, during 2002 to 2019, by a similar amount. Stations at which *in situ* NPP exceeded 700 mg C m^{-2} d^{-1} exhibited an underestimation in MODIS-A Chl *a*, whereas the remaining stations both over and under estimated satellite Chl *a*.

The PSM showed a systematic bias (Fig. 3) resulting in a higher underestimation of NPP compared to the WRM and VGPM. The photosynthetic parameters, P^B_m and α^B, used to parameterise the rate of photosynthesis in the PSM, are not used in the other models. Our data suggest that the regionally-averaged values of these parameters used in this study may be underestimated for the South Atlantic. Dogliotti et al. (2014) reported that the PSM performed well on the Patagonian Shelf when using *in situ* P^B_m and α^B, collected at the same time as Chl *a* data used for validation of NPP algorithms, but it is not possible to run the PSM at the basin scale in this way. To assess this further, the PSM was run using *in situ* P^B_m and α^B from the season and province of each individual station, but there was no improvement and an even higher systematic bias (M = 0.37, log-RMS = 0.41, $N = 17$), indicating that the variability in the two photosynthetic parameters is not sufficiently represented by the available *in situ* data for the South Atlantic (Bouman et al., 2018; Platt and Sathyendranath, 1988).

4.1.3. Accuracy assessment of NCP

The NCP algorithms tested in this study are still in their infancy compared to NPP models, but the results are promising. Running the NCP algorithms with *in situ* NPP and SST showed that NCP-C performs slightly better than NCP-D (Table 4). This contrasts with Tilstone et al. (2015a), who found that over the entire Atlantic Ocean NCP-D was more accurate since it includes a temperature function which theoretically captures more of the natural variability in respiration rates. Howard et al. (2017) observed net autotrophic conditions in the SATL during austral autumn, which are also represented more accurately by NCP-C, but observed NCP closer to estimates of NCP-D in the SSTC. Serret et al. (2015) highlighted that NCP is not just determined by NPP, with a heterogeneous relationship between NPP and respiration and substantial differences between the North and South Atlantic. The relationship between NPP and respiration could also change with the season (Serret et al., 2015), while the majority of the calibration data for NCP-C and NCP-D occurs in austral spring. Using satellite data alone however, NCP-D was the best performing algorithm (Table 5), and when driven with *in situ* NPP the differences to NCP-C were small.

Table 6
Perturbation analysis results showing the percentage reduction in NCP-D log-RMS under different scenarios as described in Section 2.10.

Scenario	Percentage reduction in log-RMS
Chl *a*	22%
SST	3.5%
PAR	2.8%
NPP	40%
in situ NCP	36%
All Input	61%
All Input and *in situ* NCP	87%

The first five scenarios use single parameter perturbations to determine the individual reductions in log-RMS when accounting for the uncertainties. The further two scenarios determine the reduction in log-RMS when firstly all input parameters (Chl *a*, PAR, SST and NPP) are perturbed by their uncertainties, and secondly when all input parameters and the *in situ* NCP uncertainties are perturbed.

Table 5
Performance indices for satellite net community production (NCP) algorithms. To log transform negative NCP values, we added the minimum value (−170 mmol O_2 $m^{-2}d^{-1}$) to all values.

Weighted											
Model	R^2	Slope	Intercept	Log-RMS	APD	M	S	F_{min}	F_{med}	F_{max}	N
A	0.54	**0.99**	−0.11	0.48	14.4	0.33	0.34	**0.97**	2.14	4.70	14
B	0.64	0.96	0.04	**0.10**	**3.4**	**0.01**	**0.10**	0.81	**1.03**	**1.30**	14
C	0.62	0.96	**0.01**	**0.12**	**4.5**	0.07	**0.10**	0.93	1.17	1.48	14
D	**0.70**	**0.98**	**0.00**	**0.11**	**3.5**	0.06	**0.09**	0.93	1.14	1.40	14

Log-differences uncertainties in satellite estimates are mean (M), standard deviation (S) and Root Mean Square (log-RMS). The mean and one sigma range of the difference are given as; F_{med}, F_{min} and F_{max}; values closer to 1 indicate greater accuracy. APD is the Absolute Percentage Difference. N indicates the number of matchups used to compute statistics. The most accurate algorithm for each statistic is highlighted in bold. Statistics were computed by weighting each station based on the *in situ* and satellite uncertainty (weighted).

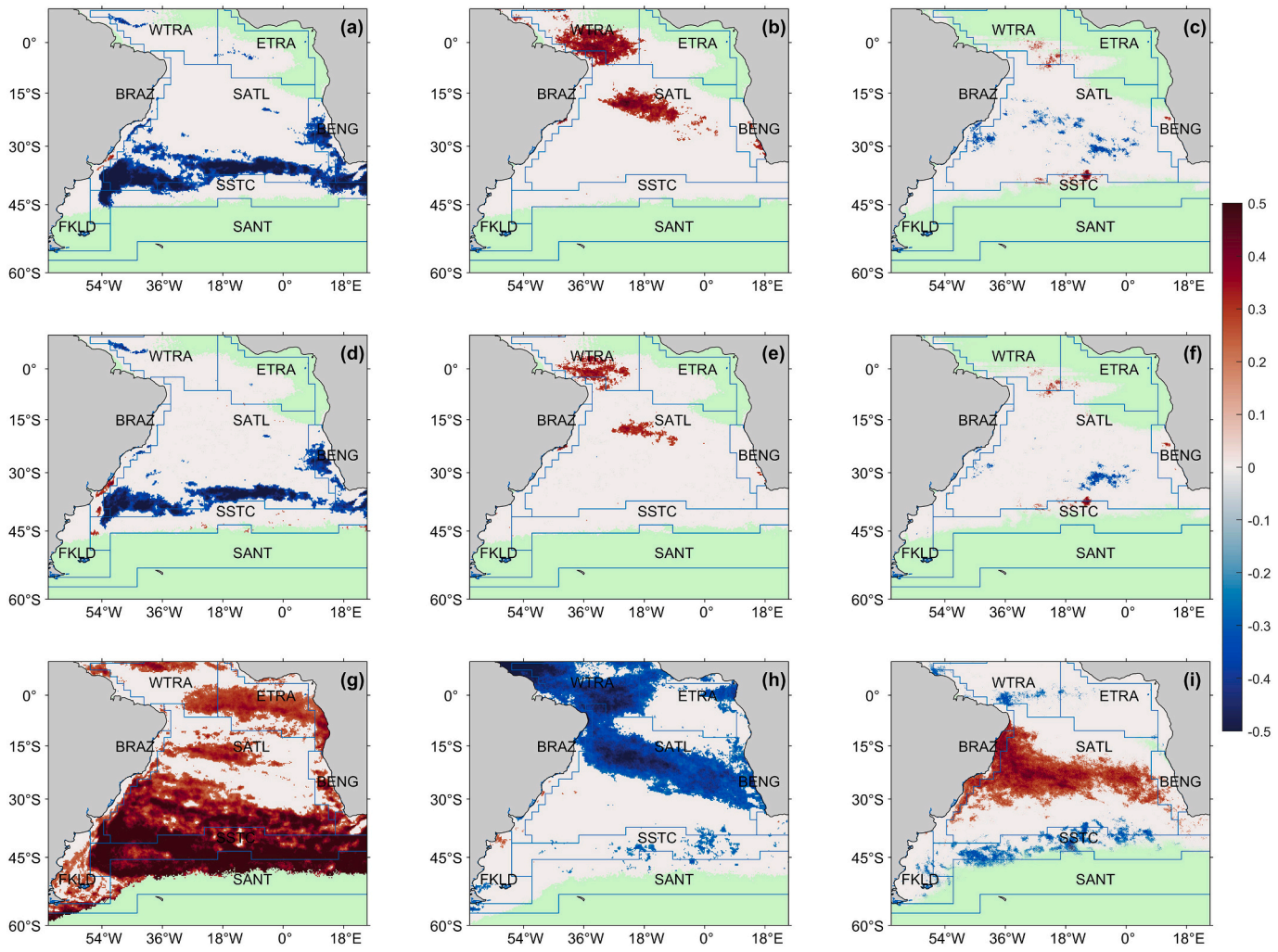

Fig. 6. Significant per pixel Spearman correlations between monthly satellite net community production (NCP-D) anomalies and (a) sea level height anomaly, (b) wind speed anomaly and (c) Multivariate ENSO Index (MEI). (d), (e) and (f) show the same for monthly satellite net primary production (WRM) anomalies and (g), (h) and (i) for monthly satellite sea surface temperature anomalies. The correlations were deemed significant when the 95% confidence interval of the Spearman correlation, determined through a Monte Carlo uncertainty propagation, remained significant ($\alpha = 0.05$). Light grey regions indicate no significant correlation. Green areas indicate where more than 24 months of data are missing ($N = 168$ to 192). (For interpretation of the references to colour in this figure legend, the reader is referred to the web version of this article.)

4.1.4. *Weighted statistics and perturbation analysis*

In situ measurements used to assess satellite algorithm performance have their own uncertainties and cannot be assumed to be "100% accurate" as is common practice (*e.g.* Brewin et al., 2015; Dogliotti et al., 2014; Dogliotti et al., 2009). The perturbation analysis conducted in this paper showed that 36% of the NCP algorithm uncertainty could be attributed to the *in situ* NCP uncertainty (Table 6), indicating that this is the highest accuracy that a satellite NCP algorithm can currently achieve (equivalent to 0.03 $\log_{10}$ mmol O_2 m^{-2} d^{-1}). A further 61% of the uncertainty was attributed to all of the satellite input parameters (Table 6), reinforcing the need to account for *in situ* as well as satellite uncertainties when assessing satellite algorithm performance, and therefore to use weighted statistics to account for the uncertainties in both the *in situ* data used to evaluate algorithm performance, and the satellite data used to run the algorithm. Differences between the unweighted and weighted statistics are clearer for discrete station measurements, such as NPP (Table 3; Appendix 1 Table A2) and NCP (Tables 4, 5; Appendix 1 Table A3 A4), where uncertainties are unlikely to be constant.

Large *in situ* datasets have been compiled for Chl *a* to test the performance of satellite algorithms (*e.g.* Valente et al., 2016, 2019). These datasets contain discrete station measurements across the globe, but do not include the associated uncertainties. A weighted approach could also be expanded for algorithm development, where uncertainties in both the *in situ* calibration and validation datasets could also be used to evaluate the algorithm performance.

Uncertainties in the satellite data make the largest contribution to the total uncertainty. In this study we have not included the uncertainties associated with atmospheric correction and the resulting satellite R_{rs} (Li et al., 2019). Land et al. (2018) proposed a promising statistical approach to estimate some of these uncertainties in Chl *a* alone. This is beyond the scope of this study, but is an important topic to pursue in the future to trace the uncertainties in R_{rs} through Chl *a* to NPP

to NCP.

4.2. Climate indices and environmental drivers of NCP

Applying the most accurate satellite NCP and input parameter algorithms to the 16 year MODIS-A time series, enables the exploration of climate indices and environmental drivers that may modulate NCP in the South Atlantic. Tilstone et al. (2015a) showed correlations between monthly province-averaged NCP anomalies and climate indices for the SeaWiFS time series between 1998 and 2010 in the Atlantic Ocean.

Conducting the correlation analysis on province-averaged NCP anomalies, between 2002 and 2018, we showed no significant correlations between NCP anomalies and wind speed anomalies, SLHA and the climate indices, when the NCP uncertainties were accounted for. Tilstone et al. (2015a) showed significant correlation between NCP anomalies and the MEI in the SATL, which may become non-significant if the uncertainties are accounted for. Correlations with the environmental drivers at local scales may however, still be significant. This was therefore studied in more detail, by conducting a correlation analysis on a per pixel basis across the region (Fig. 6). This technique has previously proved effective for determining trends in phytoplankton pigments and production (*e.g.*: Behrenfeld et al., 2006; Dunstan et al., 2018; Kahru et al., 2010).

Significant positive correlations were found between wind speed and NCP anomalies, along the BENG coast (Fig. 6b). An increase in upwelling conducive wind speeds enhances the upwelling of colder, nutrient rich waters, causing an increase in NPP (Chen et al., 2012; Lamont et al., 2019) and therefore potentially in NCP. The negative correlations between wind speed and SST anomalies (Fig. 6h) indicate the enhancement of nutrient rich, cold water at the surface, under elevated wind speeds, which in turn drive the correlations between wind speed and NPP anomalies (Fig. 6e).

Negative correlations between NCP anomalies and SLHA were observed offshore in the BENG, extending into the SATL (Fig. 6a). SLHA show substantial mesoscale activity in the form of eddies and filaments that propagate away from the upwelling front and advect more productive, cooler waters (negative SLHA; positive NCP anomalies) into the SATL (Rubio et al., 2009). The positive correlations between SST anomalies and SLHA (Fig. 6g; negative SST anomalies; negative SLHA) extended offshore of the BENG, but to a lesser extent than negative correlations between NPP anomalies and SLHA (Fig. 6d). Rubio et al. (2009) indicated that these eddies and filaments can advect a significant volume of nutrient rich water into the SATL, which potentially enhances NPP and NCP offshore. Lamont et al. (2019) showed that long-term trends in Chl *a* and phytoplankton size structure differed between open ocean ($>$ 1000 m) and shelf ($<$ 1000 m) regions of the BENG, suggesting different driving mechanisms between shelf and open ocean regions.

In the SATL, an area of positive correlations between NCP anomalies and wind speed anomalies were observed (Fig. 6b). Productivity in this region is influenced by the equatorial upwelling and South Equatorial current, both of which are wind-driven (Hooker et al., 2000). Wind speed anomalies were positively correlated with both NPP and NCP anomalies (Fig. 6b), suggesting a connection between wind induced mixing of nutrients to the photic zone which in turn fuels NPP and NCP. Negative correlations between SST anomalies and wind speed anomalies have a larger regional influence (Fig. 6h) than correlations with NCP and NPP anomalies (Fig. 6b, e).

In the SSTC, significant negative correlations between NCP anomalies and SLHA were observed, extending north into the SATL (Fig. 6a). From 30° S to 40° S, the western region between 54° W and 36° W, is influenced by mesoscale eddies from the Brazil-Malvinas confluence, where the deflection of the two currents generates, anticyclonic (positive SLHA; negative NCP anomalies) and cyclonic (negative SLHA; positive NCP anomalies) eddies (Garcia et al., 2004).

The leakage of Indian Ocean waters into the South Atlantic is facilitated by Agulhas eddies, shed from the Agulhas Current, at the southern tip of South Africa (Guerra et al., 2018). These rings propagate across the South Atlantic, reaching the Brazilian coast between 15° S and 30° S. A band of significant positive correlations between SST anomalies and SLHA (Fig. 6g), are an indication of the presence of mesoscale eddies, which start at the southern tip of Africa, and end near the Brazilian coast. This is consistent with the basin-scale propagation of these Agulhas rings. These rings are anticyclonic 'warm' eddies, generally associated with positive SLHA, which induce downwelling of nutrients that potentially decreases NPP (He et al., 2016). The response of the plankton community to these Agulhas eddies in both NPP and NCP anomalies is clear at the southern tip of Africa, with negative correlations between NPP/NCP anomalies and SLHA (Fig. 6a, d; positive SLHA; negative NPP/NCP anomalies). The response in NPP and NCP as these Agulhas eddies propagate across the South Atlantic is less clear however, with some patchy negative correlations between NCP anomalies and SLHA (Fig. 6a), and to a lesser extent between NPP anomalies and SLHA (Fig. 6d). The influence of oceanic mesoscale eddies on phytoplankton production varies with the structure and age of the feature (Liu et al., 2018; Nencioli et al., 2018).

On a per pixel basis, patchy negative correlations between NCP anomalies and the MEI were observed in the SATL (Fig. 6c), reciprocated in correlations between NPP anomalies and the MEI (Fig. 6f). El Niño periods are coupled with variability in SST in the South Atlantic, leading to higher temperatures in the SATL (Rodrigues et al., 2015), which are evident in the positive correlations between SST anomalies and the MEI in this region (Fig. 6i). Higher SST in the SATL is associated with stronger stratification and decreased nutrient supply, which can reduce NPP and NCP, but this was not seen in our analysis of the South Atlantic.

Future climate change effects could drive changes in environmental forcing, which we have shown to control the metabolic state of the South Atlantic. Oceanic wind speeds have increased from 1985 to 2018 (Young and Ribal, 2019) and if this trend continues, it may suggest that areas of the South Atlantic become more autotrophic, driven by nutrient enrichment from upwelling and water column mixing. Upwelling favourable winds may become more prevalent along eastern boundary upwelling systems (Aguirre et al., 2019), inducing a further increase in these autotrophic communities in the Benguela system.

5. Conclusions

In this paper, we perform a comprehensive uncertainty analysis of ocean colour parameters for MODIS-A in the South Atlantic Ocean, to enable the generation of an accurate satellite NCP time series, to investigate the effect of environmental drivers on NCP. Five Chl *a*, three NPP and four NCP satellite algorithms were assessed using a weighted statistical analysis which takes into account the uncertainty in both the satellite and *in situ* data. For Chl *a*, OC3-CI showed the best performance, however all algorithms showed a large underestimation at higher Chl *a* concentrations. For NPP, the WRM showed the best performance, however it underestimated NPP at more productive stations. For NCP, NCP-D showed the highest accuracy and NCP-C was also similar. Up to 61% of the uncertainty in satellite NCP could be attributed to uncertainties in the input parameters. The uncertainties in the NPP model (40%) and Chl *a* (22%) accounted for the greatest reduction in the log-RMS, indicating that these need to be reduced to improve the derivation

of NCP using satellite data.

Using NCP-D, in conjunction with the most accurate input parameters, a 16 year monthly time series of NCP anomalies was produced for the South Atlantic Ocean, to investigate the effect of climate indices and environmental drivers on NCP. The central SATL showed significant positive correlations between wind speed and NCP anomalies. Similarly, in the Benguela region, significant positive correlations between wind speed and NCP anomalies dominated the coastal regions, indicating that wind driven upwelling controls autotrophic NCP in this region. Offshore SLHA had significant negative correlation with NCP anomalies which extended into the South Atlantic gyre. This correlation suggests that the propagation of mesoscale eddies and filaments from the BENG, modifies the autotrophic metabolic state of the plankton community offshore and into the SATL. Significant negative correlations between NCP anomalies and SLHA were also observed at the southern tip of Africa, highlighting that anticyclonic Agulhas Current rings and their associated fronts modify NCP in this region. Significant negative correlations between SLHA and NCP anomalies also occur in the Brazil-Malvinas Confluence region through persistent eddy generation.

Declaration of Competing Interest

The authors declare that they have no known competing financial interests or personal relationships that could have appeared to influence the work reported in this paper.

Acknowledgements

DF was supported by a GW4+ Doctoral Training Partnership studentship from the UK Natural Environment Research Council (NERC; NE/L002434/1). GT was supported by the AMT4SentinelFRM (ESRIN/RFQ/3-14457/16/I-BG) and AMT4OceanSatFlux (4000125730/18/NL/FF/gp) contracts from the European Space Agency and by NERC National Capability funding to Plymouth Marine Laboratory for the Atlantic Meridional Transect (AMT). PL was supported by SPBU travel grant # 41128672. GT and MK were also funded by NERC International Opportunity Fund Grant Satellite estimates of marine net community production in the South Atlantic from Sentinel-3 (SemSAS; NE/P00878X/1). MK was partially funded by P&D ANP/BRASOIL Project no. 48610.011013/2014-66; Dalio Foundation Proj. Amazon Reefs. FB and MC were supported by four Oceanographic Institute of the University of São Paulo (IOUSP) projects (FAPESP 2015/01373-0; CNPq 442926/2015-4; FAPESP 2014/50820-7; CNPq 565060/2010-4) for the collection of the Chl *a* data used in the BRAZ dataset. We would like to thank the captain and crew of *RRS Discovery, RRS James Clark Ross and RRS James Cook* for conducting the AMTs. We also thank the Natural Environment Research Council Earth Observation Data Acquisition and Analysis Service (NEODAAS) for use of the Linux cluster to process the MODIS-A satellite imagery. The altimeter products were produced by Ssalto/Duacs and distributed by Aviso+, with support from Cnes (https://www.aviso.altimetry.fr). The AMT is funded by NERC through its National Capability Long-term Single Centre Science Programme, Climate Linked Atlantic Sector Science (NE/R015953/1). This study contributes to the international IMBeR project and is contribution number 354 of the AMT programme.

Appendices. Appendix 1 – Unweighted Statistics

Table A1

Performance indices for satellite chlorophyll *a* algorithms using AMT dataset. Log-differences uncertainties in satellite estimates are mean (M), standard deviation (S) and Root Mean Square (log-RMS). The mean and one sigma range of the difference are given as; F_{med}, F_{min} and F_{max}; values closer to 1 indicate greater accuracy. APD is the Absolute Percentage Difference. N indicates the number of matchups used to compute statistics. Statistics were computed using a standard unweighted procedure.

Unweighted												
	Model	R^2	Slope	Intercept	log-RMS	APD	M	S	F_{min}	F_{med}	F_{max}	N
AMT	OC3-CI	0.94	0.92	-0.14	0.15	125	0.07	0.14	0.85	1.17	1.60	1440
	OC3	0.92	0.91	-0.14	0.16	126	0.06	0.15	0.80	1.14	1.63	1440
	GSM	0.92	0.94	-0.15	0.18	143	0.09	0.15	0.87	1.24	1.75	1440
	OC5	0.92	0.86	-0.21	0.18	162	0.09	0.16	0.84	1.22	1.77	1440
	OC5-CI	0.93	0.87	-0.21	0.17	161	0.09	0.14	0.89	1.24	1.73	1440

Table A2

Performance indices for satellite net primary production algorithms. Log-differences uncertainties in satellite estimates are mean (M), standard deviation (S) and Root Mean Square (log-RMS). The mean and one sigma range of the difference are given as; F_{med}, F_{min} and F_{max}; values closer to 1 indicate greater accuracy. APD is the Absolute Percentage Difference. N indicates the number of matchups used to compute statistics. Statistics were computed using a standard unweighted procedure.

	Unweighted										
Model	R^2	Slope	Intercept	log-RMS	APD	M	S	F_{min}	F_{med}	F_{max}	N
VGPM	0.68	0.86	0.33	0.23	7.4	0.02	0.23	0.62	1.05	1.79	18
PSM	0.78	0.76	0.37	0.31	9.7	0.24	0.20	1.12	1.75	2.75	18
WRM	0.71	0.91	0.16	0.22	7.6	0.06	0.22	0.69	1.15	1.90	18

Table A3
Performance indices for net community production (NCP) algorithms driven by *in situ* net primary production and *in situ* sea surface temperature. To log transform negative NCP values, we add the minimum value (-170 mmol O_2 $m^{-2}d^{-1}$) to all values. Log-differences uncertainties in satellite estimates are mean (M), standard deviation (S) and Root Mean Square (log-RMS). The mean and one sigma range of the difference are given as; F_{med}, F_{min} and F_{max}; values closer to 1 indicate greater accuracy. APD is the Absolute Percentage Difference. N indicates the number of matchups used to compute statistics. Statistics were computed using a standard unweighted procedure.

					Unweighted						
Model	R^2	Slope	Intercept	log-RMS	APD	M	S	F_{min}	F_{med}	F_{max}	N
A	0.14	3.00	-4.93	0.53	18.2	0.39	0.36	1.08	2.48	5.70	84
B	0.23	0.53	1.11	0.12	3.8	-0.05	0.11	0.69	0.89	1.16	84
C	0.23	0.74	0.58	0.12	3.9	0.00	0.12	0.76	0.99	1.31	84
D	0.21	0.95	0.10	0.13	4.6	0.01	0.13	0.75	1.02	1.38	84

Table A4
Performance indices for satellite net community production (NCP) algorithms. To log transform negative NCP values, we added the minimum value (-170 mmol O_2 $m^{-2}d^{-1}$) to all values. Log-differences uncertainties in satellite estimates are mean (M), standard deviation (S) and Root Mean Square (log-RMS). The mean and one sigma range of the difference are given as; F_{med}, F_{min} and F_{max}; values closer to 1 indicate greater accuracy. APD is the Absolute Percentage Difference. N indicates the number of matchups used to compute statistics. Statistics were computed using a standard unweighted procedure.

					Unweighted						
Model	R^2	Slope	Intercept	log-RMS	APD	M	S	F_{min}	F_{med}	F_{max}	N
A	0.35	3.53	-6.32	0.79	27.0	0.59	0.54	1.12	3.92	13.69	14
B	0.50	0.48	1.20	0.13	4.6	-0.03	0.13	0.69	0.94	1.27	14
C	0.49	0.69	0.65	0.13	5.0	0.05	0.13	0.84	1.12	1.50	14
D	0.61	0.81	0.40	0.11	4.0	0.04	0.11	0.85	1.10	1.42	14

Appendix 2 – Chl-a Statistics for BRAZ and BEN datasets

Table A5
Performance indices for satellite chlorophyll *a* algorithms using BRAZIL dataset. Log-differences uncertainties in satellite estimates are mean (M), standard deviation (S) and Root Mean Square (log-RMS). The mean and one sigma range of the difference are given as; F_{med}, F_{min} and F_{max}; values closer to 1 indicate greater accuracy. APD is the Absolute Percentage Difference. N indicates the number of matchups used to compute statistics. Statistics were computed firstly assuming all stations have equal weighting (unweighted) and secondly weighting each station based only on the satellite uncertainty (ɛC) (weighted).

Unweighted												
	Model	R^2	Slope	Intercept	log-RMS	APD	M	S	F_{min}	F_{med}	F_{max}	N
BRAZIL	OC3-CI	0.83	0.90	-0.15	0.13	35	0.07	0.12	0.88	1.16	1.53	30
	OC3	0.73	1.07	-0.03	0.19	38	0.09	0.16	0.85	1.24	1.80	30
	GSM	0.22	1.01	-0.22	0.38	104	0.23	0.30	0.85	1.71	3.42	30
	OC5	0.72	0.96	-0.16	0.20	46	0.13	0.16	0.94	1.35	1.93	30
	OC5-CI	0.86	0.78	-0.27	0.15	42	0.09	0.12	0.94	1.24	1.63	30

Weighted												
	Model	R^2	Slope	Intercept	log-RMS	APD	M	S	F_{min}	F_{med}	F_{max}	N
BRAZIL	OC3-CI	0.86	1.00	-0.06	0.13	39	0.08	0.11	0.92	1.19	1.54	30
	OC3	0.81	0.94	-0.09	0.15	39	0.07	0.13	0.86	1.17	1.58	30
	GSM	0.43	1.04	-0.10	0.26	38	0.16	0.21	0.90	1.45	2.32	30
	OC5	0.81	0.87	-0.17	0.17	48	0.11	0.13	0.95	1.28	1.72	30
	OC5-CI	0.88	0.91	-0.14	0.14	44	0.09	0.11	0.97	1.24	1.59	30

Table A6
Performance indices for satellite chlorophyll *a* algorithms using BEN dataset. Log-differences uncertainties in satellite estimates are mean (M), standard deviation (S) and Root Mean Square (log-RMS). The mean and one sigma range of the difference are given as; F_{med}, F_{min} and F_{max}; values closer to 1 indicate greater accuracy. APD is the Absolute Percentage Difference. N indicates the number of matchups used to compute statistics. Statistics were computed firstly assuming all stations have equal weighting (unweighted) and secondly weighting each station based only on the satellite uncertainty (ƐC) (weighted).

Unweighted												
	Model	R^2	Slope	Intercept	log-RMS	APD	M	S	F_{min}	F_{med}	F_{max}	N
BEN	OC3-CI	0.74	0.92	0.00	0.28	108	0.02	0.28	0.55	1.05	2.00	38
	OC3	0.75	0.94	-0.01	0.28	108	0.02	0.28	0.55	1.06	2.02	38
	GSM	0.69	1.10	0.09	0.35	109	-0.11	0.34	0.36	0.78	1.71	38
	OC5	0.76	0.85	-0.11	0.30	103	0.14	0.27	0.74	1.37	2.57	38
	OC5-CI	0.76	0.84	-0.10	0.30	103	0.14	0.27	0.73	1.37	2.56	38

Weighted												
	Model	R^2	Slope	Intercept	log-RMS	APD	M	S	F_{min}	F_{med}	F_{max}	N
BEN	OC3-CI	0.80	0.92	-0.02	0.25	89	0.03	0.25	0.61	1.08	1.93	38
	OC3	0.80	0.94	-0.03	0.25	89	0.04	0.25	0.61	1.09	1.95	38
	GSM	0.75	1.00	0.05	0.30	92	-0.06	0.30	0.44	0.86	1.71	38
	OC5	0.80	0.87	-0.10	0.29	94	0.14	0.25	0.78	1.39	2.48	38
	OC5-CI	0.80	0.86	-0.10	0.29	94	0.14	0.25	0.78	1.38	2.47	38

Appendix 3 – Satellite skin sea surface temperature uncertainty

Sea surface temperature (SST) is a key variable for both NPP and NCP algorithms, and therefore the performance of MODIS-A SST retrievals were assessed. SST measurements by infrared radiometers, such as MODIS-A, are a measurement of the SST at the oceans skin (~10 μm), but are usually compared to *in situ* buoy measurements of temperature below the surface (~5 m). These temperature measurements can introduce additional uncertainty through vertical temperature gradients in the water column, and therefore a measurement of skin SST should be used in determining the uncertainty of MODIS-A SST.

Skin SST measurements made on three AMT cruise in 2017, 2018 and 2019 (AMT 27, 28, 29) using an infrared SST autonomous radiometer (ISAR) as outlined in Donlon et al. (2008), were downloaded from the Ships4SST website (http://ships4sst.org/). Each individual measurement was provided with an uncertainty using the statistical model outlined in Wimmer and Robinson (2016).

In situ measurements were subjected to the same matchup protocol as the ocean colour component, as described in Section 2.7. Satellite uncertainties were determined following the same approach as the ocean colour component, with Ɛi assumed to be negligible, and Ɛa assigned a value of 0.345 °C (Brown and Minnett, 1999).

Weighted linear regression analysis is shown in Fig. A1 with associated statistics tabulated in Table A7. Our results show MODIS-A SST measurements are accurate having no bias and little scatter, falling on the 1:1 line.

Table A7
Performance indices for satellite sea surface temperature (SST). Log-differences uncertainties in satellite estimates are mean (M) and standard deviation (S). Root Mean Square Error (RMS) was computed as opposed to log-RMS. The mean and one sigma range of the difference are given as; F_{med}, F_{min} and F_{max}; values closer to 1 are more accurate. APD is the Absolute Percentage Difference. N indicates the number of matchups used to compute statistics. Statistics were computed firstly assuming all stations have equal weighting (unweighted) and secondly weighting each station based on the *in situ* and satellite uncertainty (weighted).

Unweighted											
	R^2	Slope	Intercept	RMS	APD	M	S	F_{min}	F_{med}	F_{max}	N
SST	0.99	1.01	-0.16	0.41	1.4	0.00	0.01	0.98	1.00	1.02	362
Weighted											
	R^2	Slope	Intercept	RMS	APD	M	S	F_{min}	F_{med}	F_{max}	N
SST	0.99	1.00	-0.08	0.41	1.4	0.00	0.01	0.98	1.00	1.02	362

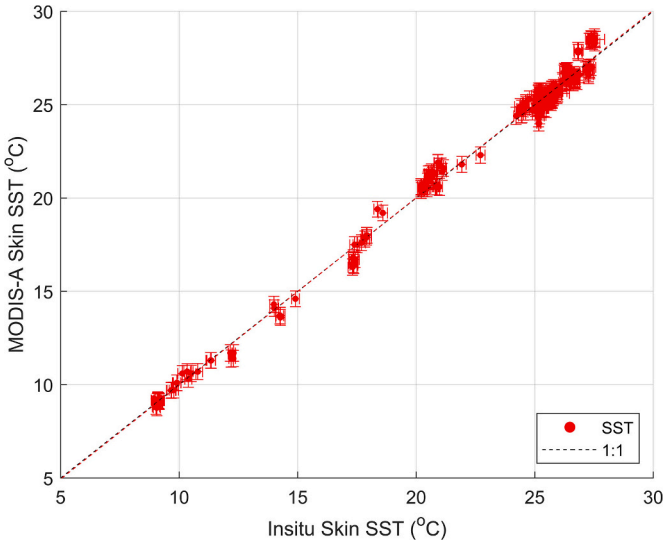

Fig. A1. Comparison of ISAR and MODIS-A skin sea surface temperature (SST). Black dashed line is the 1:1 line. Red dashed line is a weighted Type-II linear regression between the ISAR and MODIS-A skin SST. Horizontal error bars indicate *in situ* uncertainty (Εins). Vertical error bars indicate the combined satellite uncertainty (ΕC).

References

Aguirre, C., Rojas, M., Garreaud, R.D., Rahn, D.A., 2019. Role of synoptic activity on projected changes in upwelling-favourable winds at the ocean's eastern boundaries. NPJ Clim. Atmos. Sci. 2, 44. https://doi.org/10.1038/s41612-019-0101-9.

Bailey, S.W., Werdell, P.J., 2006. A multi-sensor approach for the on-orbit validation of ocean color satellite data products. Remote Sens. Environ. 102, 12–23. https://doi.org/10.1016/j.rse.2006.01.015.

Barlow, R.G., Cummings, D.G., Gibb, S.W., 1997. Improved resolution of mono- and divinyl chlorophylls *a* and *b* and zeaxanthin and lutein in phytoplankton extracts using reverse phase C-8 HPLC. Mar. Ecol. Prog. Ser. 161, 303–307. https://doi.org/10.1016/j.dsr.2007.06.010.

Behrenfeld, M.J., Falkowski, P.G., 1997. Photosynthetic rates derived from satellite-based chlorophyll concentration. Limnol. Oceanogr. 42, 1–20. https://doi.org/10.4319/lo.1997.42.1.0001.

Behrenfeld, M.J., O'Malley, R.T., Siegel, D.A., McClain, C.R., Sarmiento, J.L., Feldman, G.C., Milligan, A.J., Falkowski, P.G., Letelier, R.M., Boss, E.S., 2006. Climate-driven trends in contemporary ocean productivity. Nature 444, 752–755. https://doi.org/10.1038/nature05317.

BIPM, 2008. Evaluation of measurement data—guide to the expression of uncertainty in measurement. JCGM 100. http://www.bipm.org/utils/common/documents/jcgm/JCGM_100_2008_E.pdf.

Bouman, H.A., Platt, T., Doblin, M., Figueiras, F.G., Gudmundsson, K., Gudfinnsson, H. G., Huang, B., Hickman, A., Hiscock, M., Jackson, T., Lutz, V.A., Mélin, F., Rey, F., Pepin, P., Segura, V., Tilstone, G.H., van Dongen-Vogels, V., Sathyendranath, S., 2018. Photosynthesis–irradiance parameters of marine phytoplankton: synthesis of a global data set. Earth Syst. Sci. Data 10, 251–266. https://doi.org/10.5194/essd-10-251-2018.

Brewin, R.J.W., Sathyendranath, S., Müller, D., Brockmann, C., Deschamps, P.Y., Devred, E., Doerffer, R., Fomferra, N., Franz, B., Grant, M., Groom, S., Horseman, A., Hu, C., Krasemann, H., Lee, Z.P., Maritorena, S., Mélin, F., Peters, M., Platt, T., Regner, P., Smyth, T., Steinmetz, F., Swinton, J., Werdell, J., White, G.N., 2015. The ocean colour climate change initiative: III. A round-robin comparison on in-water bio-optical algorithms. Remote Sens. Environ. 162, 271–294. https://doi.org/10.1016/j.rse.2013.09.016.

Brewin, R.J.W., Dall'Olmo, G., Pardo, S., van Dongen-Vogels, V., Boss, E.S., 2016. Underway spectrophotometry along the Atlantic Meridional transect reveals high performance in satellite chlorophyll retrievals. Remote Sens. Environ. https://doi.org/10.1016/j.rse.2016.05.005.

Brown, O.B., Minnett, P.J., 1999. MODIS Infrared Sea Surface Temperature Algorithm.

Campbell, J., Antoine, D., Armstrong, R., Arrigo, K., Balch, W., Barber, R., Behrenfeld, M., Bidigare, R., Bishop, J., Carr, M.-E., Esaias, W., Falkowski, P., Hoepffner, N., Iverson, R., Kiefer, D., Lohrenz, S., Marra, J., Morel, A., Ryan, J., Vedernikov, V., Waters, K., Yentsch, C., Yoder, J., 2002. Comparison of algorithms for estimating ocean primary production from surface chlorophyll, temperature, and irradiance. Global Biogeochem. Cycles 16. https://doi.org/10.1029/2001GB001444, 9-1-9-15.

Carr, M.E., Friedrichs, M.A.M., Schmeltz, M., Noguchi Aita, M., Antoine, D., Arrigo, K.R., Asanuma, I., Aumont, O., Barber, R., Behrenfeld, M., Bidigare, R., Buitenhuis, E.T., Campbell, J., Ciotti, A., Dierssen, H., Dowell, M., Dunne, J., Esaias, W., Gentili, B., Gregg, W., Groom, S., Hoepffner, N., Ishizaka, J., Kameda, T., Le Quéré, C., Lohrenz, S., Marra, J., Mélin, F., Moore, K., Morel, A., Reddy, T.E., Ryan, J., Scardi, M., Smyth, T., Turpie, K., Tilstone, G., Waters, K., Yamanaka, Y., 2006. A comparison of global estimates of marine primary production from ocean color. Deep. Res. Part II Top. Stud. Oceanogr. 53, 741–770. https://doi.org/10.1016/j.dsr2.2006.01.028.

Chang, C.H., Johnson, N.C., Cassar, N., 2014. Neural network-based estimates of Southern Ocean net community production from in situ O_2/Ar and satellite observation: a methodological study. Biogeosciences 11, 3279–3297. https://doi.org/10.5194/bg-11-3279-2014.

Chen, Z., Yan, X.H., Jo, Y.H., Jiang, L., Jiang, Y., 2012. A study of Benguela upwelling system using different upwelling indices derived from remotely sensed data. Cont. Shelf Res. 45, 27–33. https://doi.org/10.1016/j.csr.2012.05.013.

Dall'Olmo, G., Westberry, T.K., Behrenfeld, M.J., Boss, E., Slade, W.H., 2009. Significant contribution of large particles to optical backscattering in the open ocean. Biogeosciences. https://doi.org/10.5194/bg-6-947-2009.

Dall'Olmo, G., Boss, E., Behrenfeld, M.J., Westberry, T.K., 2012. Particulate optical scattering coefficients along an Atlantic Meridional transect. Opt. Express 20, 21532. https://doi.org/10.1364/OE.20.021532.

Dogliotti, A.I., Scientific, N., Schloss, I.R., 2009. Evaluation of SeaWiFS and MODIS chlorophyll - a products in the Argentinean Patagonian Continental Shelf (38°S – 55°S). https://doi.org/10.1080/01431160802311133.

Dogliotti, A.I., Lutz, V.A., Segura, V., 2014. Estimation of primary production in the southern argentine continental shelf and shelf-break regions using field and remote sensing data. Remote Sens. Environ. 140, 497–508. https://doi.org/10.1016/j.rse.2013.09.021.

Donlon, C., Robinson, I.S., Reynolds, M., Wimmer, W., Fisher, G., Edwards, R., Nightingale, T.J., 2008. An infrared sea surface temperature autonomous radiometer (ISAR) for deployment aboard volunteer observing ships (VOS). J. Atmos. Ocean. Technol. 25, 93–113. https://doi.org/10.1175/2007JTECHO505.1.

Dunstan, P.K., Foster, S.D., King, E., Risbey, J., O'Kane, T.J., Monselesan, D., Hobday, A. J., Hartog, J.R., Thompson, P.A., 2018. Global patterns of change and variation in sea surface temperature and chlorophyll a. Sci. Rep. 8, 1–9. https://doi.org/10.1038/s41598-018-33057-y.

Field, C.B., Behrenfeld, M.J., Randerson, J.T., Falkowski, P., 1998. Primary production of the biosphere: integrating terrestrial and oceanic components. Science 281, 237–240. https://doi.org/10.1126/science.281.5374.237.

Friedrichs, M.A.M., Carr, M.-E., Barber, R.T., Scardi, M., Antoine, D., Armstrong, R.A., Asanuma, I., Behrenfeld, M.J., Buitenhuis, E.T., Chai, F., Christian, J.R., Ciotti, A.M., Doney, S.C., Dowell, M., Dunne, J., Gentili, B., Gregg, W., Hoepffner, N., Ishizaka, J., Kameda, T., Lima, I., Marra, J., Mélin, F., Moore, J.K., Morel, A., O'Malley, R.T., O'Reilly, J., Saba, V.S., Schmeltz, M., Smyth, T.J., Tjiputra, J., Waters, K., Westberry, T.K., Winguth, A., 2009. Assessing the uncertainties of model estimates of primary productivity in the tropical Pacific Ocean. J. Mar. Syst. 76, 113–133. https://doi.org/10.1016/j.jmarsys.2008.05.010.

Garcia, C.A.E., Sarma, Y.V.B., Mata, M.M., Garcia, V.M.T., 2004. Chlorophyll variability and eddies in the Brazil-Malvinas confluence region. Deep. Res. Part II Top. Stud. Oceanogr. https://doi.org/10.1016/j.dsr2.2003.07.016.

Garcia, C.A.E., Garcia, V.M.T., McClain, C.R., 2005. Evaluation of SeaWiFS chlorophyll algorithms in the southwestern Atlantic and southern oceans. Remote Sens. Environ. https://doi.org/10.1016/j.rse.2004.12.006.

Garver, S.A., Siegel, D.A., 1997. Inherent optical property inversion of ocean color spectra and its biogeochemical interpretation: 1. Time series from the Sargasso Sea. J. Geophys. Res. Ocean. 102, 18607–18625. https://doi.org/10.1029/96JC03243.

Gist, N., Serret, P., Woodward, E.M.S., Chamberlain, K., Robinson, C., 2009. Seasonal and spatial variability in plankton production and respiration in the subtropical gyres of the Atlantic Ocean. Deep. Res. Part II Top. Stud. Oceanogr. 56, 931–940. https://doi.org/10.1016/j.dsr2.2008.10.035.

Gohin, F., Druon, J.N., Lampert, L., 2002. A five channel chlorophyll concentration algorithm applied to SeaWiFS data processed by SeaDAS in coastal waters. Int. J. Remote Sens. 23, 1639–1661. https://doi.org/10.1080/01431160110071879.

Gregg, W.W., Carder, K.L., 1990. A simple spectral solar irradiance model for cloudless maritime atmospheres. Limnol. Oceanogr. https://doi.org/10.4319/lo.1990.35.8.1657.

Guerra, L.A.A., Paiva, A.M., Chassignet, E.P., 2018. On the translation of Agulhas rings to the western South Atlantic Ocean. Deep. Res. Part I Oceanogr. Res. Pap. 139, 104–113. https://doi.org/10.1016/j.dsr.2018.08.005.

He, Q., Zhan, H., Cai, S., Li, Z., 2016. Eddy effects on surface chlorophyll in the northern South China Sea: mechanism investigation and temporal variability analysis. Deep. Res. Part I Oceanogr. Res. Pap. 112, 25–36. https://doi.org/10.1016/j.dsr.2016.03.004.

Hooker, S.B., Rees, N.W., Aiken, J., 2000. An objective methodology for identifying oceanic provinces. Prog. Oceanogr. 45, 313–338. https://doi.org/10.1016/S0079-6611(00)00006-9.

Howard, E.M., Durkin, C.A., Hennon, G.M.M., Ribalet, F., Stanley, R.H.R., 2017. Biological production, export efficiency, and phytoplankton communities across 8000 km of the South Atlantic. Glob. Biogeochem. Cycles 31, 1066–1088. https://doi.org/10.1002/2016GB005488.

Hu, C., Lee, Z., Franz, B., 2012. Chlorophyll a algorithms for oligotrophic oceans: a novel approach based on three-band reflectance difference. J. Geophys. Res. Ocean. 117, 1–25. https://doi.org/10.1029/2011JC007395.

Hutchings, L., van der Lingen, C.D., Shannon, L.J., Crawford, R.J.M., Verheye, H.M.S., Bartholomae, C.H., van der Plas, A.K., Louw, D., Kreiner, A., Ostrowski, M., Fidel, Q., Barlow, R.G., Lamont, T., Coetzee, J., Shillington, F., Veitch, J., Currie, J.C., Monteiro, P.M.S., 2009. The Benguela current: an ecosystem of four components. Prog. Oceanogr. 83, 15–32. https://doi.org/10.1016/j.pocean.2009.07.046.

Kahru, M., Gille, S.T., Murtugudde, R., Strutton, P.G., Manzano-Sarabia, M., Wang, H., Mitchell, B.G., 2010. Global correlations between winds and ocean chlorophyll. J. Geophys. Res. Ocean. 115, 1–11. https://doi.org/10.1029/2010JC006500.

Kampel, M., Lorenzzetti, J.A., Bentz, C.M., Nunes, R.A., Paranhos, R., Rudorff, F.M., Politano, A.T., 2009a. Simultaneous measurements of chlorophyll concentration by lidar, fluorometry, above-water radiometry, and ocean color MODIS images in the southwestern Atlantic. Sensors 9, 528–541. https://doi.org/10.3390/s90100528.

Kampel, M., Sathyendranath, S., Platt, T., Gaeta, S.A., 2009b. Satellite estimates of phytoplankton primary production at santos bight, southwestern-south Atlantic: Comparison of algorithms. In: 2009 IEEE International Geoscience and Remote Sensing Symposium. IEEE. https://doi.org/10.1109/IGARSS.2009.5418066. II-286-II-289.

Lamont, T., Brewin, R.J.W., Barlow, R.G., 2018. Seasonal variation in remotely-sensed phytoplankton size structure around southern Africa. Remote Sens. Environ. 204, 617–631. https://doi.org/10.1016/j.rse.2017.09.038.

Lamont, T., Barlow, R.G., Brewin, R.J.W., 2019. Long-term trends in phytoplankton chlorophyll *a* and size structure in the Benguela upwelling system. J. Geophys. Res. Oceans 124, 1170–1195. https://doi.org/10.1029/2018JC014334.

Land, P.E., Bailey, T.C., Taberner, M., Pardo, S., Sathyendranath, S., Zenouz, K.N., Id, V. B., Shutler, J.D., Id, G.D.Q., 2018. A statistical modeling framework for Characterising uncertainty in large datasets : application to ocean colour. Remote Sens 10. https://doi.org/10.3390/rs10050695.

Li, J., Jamet, C., Zhu, J., Han, B., Li, T., Yang, A., Guo, K., Jia, D., 2019. Error budget in the validation of radiometric products derived from OLCI around the China Sea from open ocean to coastal waters compared with MODIS and VIIRS. Remote Sens. 11, 1997–2010. https://doi.org/10.3390/rs11202400.

Li, Z., Cassar, N., 2016. Satellite estimates of net community production based on O_2/Ar observations and comparison to other estimates. Glob. Biogeochem. Cycles 30, 735–752. https://doi.org/10.1002/2015GB005314.

Liu, F., Yin, K., He, L., Tang, S., Yao, J., 2018. Influence on phytoplankton of different developmental stages of mesoscale eddies off eastern Australia. J. Sea Res. 137, 1–8. https://doi.org/10.1016/j.seares.2018.03.004.

Lobanova, P., Tilstone, G.H., Bashmachnikov, I., Brotas, V., 2018. Accuracy assessment of primary production models with and without photoinhibition using ocean-colour climate change initiative data in the north East Atlantic Ocean. Remote Sens. 10, 1–24. https://doi.org/10.3390/rs10071116.

Longhurst, A.R., 1998. Ecological geography of the sea. Academic Press, San Diego, p. 397.

Maritorena, S., Siegel, D.A., Peterson, A.R., 2002. Optimization of a semianalytical ocean color model for global-scale applications. Appl. Opt. 41, 2705. https://doi.org/10.1364/AO.41.002705.

Maritorena, S., d'Andon, O.H.F., Mangin, A., Siegel, D.A., 2010. Merged satellite ocean color data products using a bio-optical model: characteristics, benefits and issues. Remote Sens. Environ. 114, 1791–1804. https://doi.org/10.1016/j.rse.2010.04.002.

Meister, G., Franz, B.A., 2014. Corrections to the MODIS aqua calibration derived from MODIS aqua ocean color products. IEEE Trans. Geosci. Remote Sens. 52, 6534–6541. https://doi.org/10.1109/TGRS.2013.2297233.

Morel, A., 1991. Light and marine photosynthesis: a spectral model with geochemical and climatological implications. Prog. Oceanogr. 26, 263–306. https://doi.org/10.1016/0079-6611(91)90004-6.

Morel, A., Prieur, L., 1977. Analysis of variations in ocean color. Limnol. Oceanogr. 22, 709–722. https://doi.org/10.4319/lo.1977.22.4.0709.

Morel, A., Antoine, D., Babin, M., Dandonneau, Y., 1996. Measured and modeled primary production in the Northeast Atlantic (EUMELI JGOFS program): the impact of natural variations in photosynthetic parameters on model predictive skill. Deep. Res. Part I Oceanogr. Res. Pap. https://doi.org/10.1016/0967-0637(96)00059-3.

Morel, A., Huot, Y., Gentili, B., Werdell, P.J., Hooker, S.B., Franz, B.A., 2007. Examining the consistency of products derived from various ocean color sensors in open ocean (case 1) waters in the perspective of a multi-sensor approach. Remote Sens. Environ. 111, 69–88. https://doi.org/10.1016/j.rse.2007.03.012.

NASA, 2018. MODIS-A Reprocessing R2018 [WWW Document]. URL. https://oceancolor.gsfc.nasa.gov/reprocessing/r2018/aqua/. accessed 4.29.20.

Nencioli, F., Dall'Olmo, G., Quartly, G.D., 2018. Agulhas ring transport efficiency from combined satellite altimetry and Argo profiles. J. Geophys. Res. Ocean. 123, 5874–5888. https://doi.org/10.1029/2018JC013909.

O'Reilly, J.E., Maritorena, S., Mitchell, B.G., Siegel, D.A., Carder, K.L., Garver, S.A., Kahru, M., Mcclain, C., 1998. Ocean color chlorophyll algorithms for SeaWiFS encompassing chlorophyll concentrations between. J. Geophys. Res. 103, 24937–24953.

Organelli, E., Claustre, H., 2019. Small phytoplankton shapes colored dissolved organic matter dynamics in the North Atlantic subtropical gyre. Geophys. Res. Lett. 46, 12183–12191. https://doi.org/10.1029/2019GL084699.

Platt, T., Sathyendranath, S., 1988. Oceanic primary production: estimation by remote sensing at local and regional scales. Science 241.

Platt, T., Caverhill, C., Sathyendranath, S., 1991. Basin-scale estimates of oceanic primary production by remote sensing: the North Atlantic. J. Geophys. Res. Ocean. 96, 15147–15159. https://doi.org/10.1029/91JC01118.

Poulton, A.J., Holligan, P.M., Hickman, A., Kim, Y.N., Adey, T.R., Stinchcombe, M.C., Holeton, C., Root, S., Woodward, E.M.S., 2006. Phytoplankton carbon fixation, chlorophyll-biomass and diagnostic pigments in the Atlantic Ocean. Deep. Res. Part II Top. Stud. Oceanogr. 53, 1593–1610. https://doi.org/10.1016/j.dsr2.2006.05.007.

Reed, R.K., 1977. On estimating insolation over the ocean. J. Phys. Oceanogr. 7, 482–485. https://doi.org/10.1175/1520-0485(1977)007<0482:OEIOTO>2.0.CO;2.

Rodrigues, R.R., Campos, E.J.D., Haarsma, R., 2015. The impact of ENSO on the South Atlantic subtropical dipole mode. J. Clim. 28, 2691–2705. https://doi.org/10.1175/JCLI-D-14-00483.1.

Rubio, A., Blanke, B., Speich, S., Grima, N., Roy, C., 2009. Mesoscale eddy activity in the southern Benguela upwelling system from satellite altimetry and model data. Prog. Oceanogr. 83, 288–295. https://doi.org/10.1016/j.pocean.2009.07.029.

Saba, V.S., Friedrichs, M.A.M., Antoine, D., Armstrong, R.A., Asanuma, I., Behrenfeld, M. J., Ciotti, A.M., Dowell, M., Hoepffner, N., Hyde, K.J.W., Ishizaka, J., Kameda, T., Marra, J., Mélin, F., Morel, A., O'reilly, J., Scardi, M., Smith, W.O., Smyth, T.J., Tang, S., Uitz, J., Waters, K., Westberry, T.K., 2011. An evaluation of ocean color model estimates of marine primary productivity in coastal and pelagic regions across the globe. Biogeosciences 8, 489–503. https://doi.org/10.5194/bg-8-489-2011.

Serret, P., Robinson, C., Fernández, E., Teira, E., Tilstone, G., Pérez, V., 2009. Predicting plankton net community production in the Atlantic Ocean. Deep. Res. Part II Top. Stud. Oceanogr. 56, 941–953. https://doi.org/10.1016/j.dsr2.2008.10.006.

Serret, P., Robinson, C., Aranguren-Gassis, M., García-Martín, E.E., Gist, N., Kitidis, V., Lozano, J., Stephens, J., Harris, C., Thomas, R., 2015. Both respiration and photosynthesis determine the scaling of plankton metabolism in the oligotrophic ocean. Nat. Commun. 6, 1–10. https://doi.org/10.1038/ncomms7961.

Slade, W.H., Boss, E., Dall'olmo, G., Langner, M.R., Loftin, J., Behrenfeld, M.J., Roesler, C., Westberry, T.K., 2010. Underway and moored methods for improving accuracy in measurement of spectral particulate absorption and attenuation. J. Atmos. Ocean. Technol. https://doi.org/10.1175/2010JTECHO755.1.

Smyth, T.J., Tilstone, G.H., Groom, S.B., 2005. Integration of radiative transfer into satellite models of ocean primary production. J. Geophys. Res. C Ocean. 110, 1–11. https://doi.org/10.1029/2004JC002784.

Szeto, M., Werdell, P.J., Moore, T.S., Campbell, J.W., 2011. Are the world's oceans optically different? J. Geophys. Res. Ocean. 116, 1–14. https://doi.org/10.1029/2011JC007230.

Taylor, J.R., 1997. An Introduction to Error Analysis. University Science Books, Sausalito, Calif.

Tilstone, G., Smyth, T., Poulton, A., Hutson, R., 2009. Measured and remotely sensed estimates of primary production in the Atlantic Ocean from 1998 to 2005. Deep. Res. Part II Top. Stud. Oceanogr. 56, 918–930. https://doi.org/10.1016/j.dsr2.2008.10.034.

Tilstone, G.H., Angel-Benavides, I.M., Pradhan, Y., Shutler, J.D., Groom, S., Sathyendranath, S., 2011. An assessment of chlorophyll-*a* algorithms available for SeaWiFS in coastal and open areas of the bay of Bengal and Arabian Sea. Remote Sens. Environ. 115, 2277–2291. https://doi.org/10.1016/j.rse.2011.04.028.

Tilstone, G.H., Xie, Y. Yuan, Robinson, C., Serret, P., Raitsos, D.E., Powell, T., Aranguren-Gassis, M., Garcia-Martin, E.E., Kitidis, V., 2015a. Satellite estimates of net community production indicate predominance of net autotrophy in the Atlantic Ocean. Remote Sens. Environ. 164, 254–269. https://doi.org/10.1016/j.rse.2015.03.017.

Tilstone, G.H., Taylor, B.H., Blondeau-Patissier, D., Powell, T., Groom, S.B., Rees, A.P., Lucas, M.I., 2015b. Comparison of new and primary production models using SeaWiFS data in contrasting hydrographic zones of the northern North Atlantic. Remote Sens. Environ. 156, 473–489. https://doi.org/10.1016/j.rse.2014.10.013.

Tilstone, G.H., Mallor-Hoya, S., Gohin, F., Bel, Couto A., Sa, C., Gloela, P., Cristina, S., Airs, R., Icely, J., Zuhlke, M., Groom, S.B., 2017. Which ocean colour algorithm for MERIS in NW European coastal waters? Remote Sens. Environ. 189, 132–151. https://doi.org/10.1016/j.rse.2016.11.012.

Valente, A., Sathyendranath, S., Brotas, V., Groom, S., Grant, M., Taberner, M., Antoine, D., Arnone, R., Balch, W.M., Barker, K., Barlow, R., Belanger, S., Berthon, J. F., Besiktepe, S., Brando, V., Canuti, E., Chavez, F., Claustre, H., Crout, R., Frouin, R., Garcia-Soto, C., Gibb, S.W., Gould, R., Hooker, S., Kahru, M., Klein, H., Kratzer, S.,

Loisel, H., McKee, D., Mitchell, B.G., Moisan, T., Muller-Karger, F., O'Dowd, L., Ondrusek, M., Poulton, A.J., Repecaud, M., Smyth, T., Sosik, H.M., Twardowski, M., Voss, K., Werdell, J., Wernand, M., Zibordi, G., 2016. A compilation of global bio-optical in situ data for ocean-colour satellite applications. Earth Syst. Sci. Data 8, 235–252. https://doi.org/10.5194/essd-8-235-2016.

Valente, A., Sathyendranath, S., Brotas, V., Groom, S., Grant, M., Taberner, M., Antoine, D., Arnone, R., Balch, W.M., Barker, K., Barlow, R., Bélanger, S., Berthon, J.-F., Beşiktepe, Ş., Borsheim, Y., Bracher, A., Brando, V., Canuti, E., Chavez, F., Cianca, A., Claustre, H., Clementson, L., Crout, R., Frouin, R., García-Soto, C., Gibb, S.W., Gould, R., Hooker, S.B., Kahru, M., Kampel, M., Klein, H., Kratzer, S., Kudela, R., Ledesma, J., Loisel, H., Matrai, P., McKee, D., Mitchell, B.G., Moisan, T., Muller-Karger, F., O'Dowd, L., Ondrusek, M., Platt, T., Poulton, A.J., Repecaud, M., Schroeder, T., Smyth, T., Smythe-Wright, D., Sosik, H.M., Twardowski, M., Vellucci, V., Voss, K., Werdell, J., Wernand, M., Wright, S., Zibordi, G., 2019. A compilation of global bio-optical in situ data for ocean-colour satellite applications – version two. Earth Syst. Sci. Data 11, 1037–1068. https://doi.org/10.5194/essd-11-1037-2019.

Welschmeyer, N.A., 1994. Fluorometric analysis of chlorophyll a in the presence of chlorophyll b and pheopigments. Limnol. Oceanogr. 39, 1985–1992. https://doi.org/10.4319/lo.1994.39.8.1985.

Wilks, D.S., 2006. On "field significance" and the false discovery rate. J. Appl. Meteorol. Climatol. 45, 1181–1189. https://doi.org/10.1175/JAM2404.1.

Wimmer, W., Robinson, I.S., 2016. The ISAR instrument uncertainty model. J. Atmos. Ocean. Technol. 33, 2415–2433. https://doi.org/10.1175/JTECH-D-16-0096.1.

Young, I.R., Ribal, A., 2019. Multiplatform evaluation of global trends in wind speed and wave height. Science 364, 548–552. https://doi.org/10.1126/science.aav9527.

Zapata, M., Rodríguez, F., Garrido, J., 2000. Separation of chlorophylls and carotenoids from marine phytoplankton: a new HPLC method using a reversed phase C8 column and pyridine containing mobile phases. Mar. Ecol. Prog. Ser. 195, 29–45. https://doi.org/10.3354/meps195029.